

# **NAVAL POSTGRADUATE SCHOOL**

## **Monterey, California**



## **THESIS**

**OPERATION AND CALIBRATION OF THE NPS  
ULTRAVIOLET IMAGING SPECTROMETER (NUVIS) IN  
THE DETECTION OF SULFUR DIOXIDE PLUMES**

by

Stephen A. Marino

December 1999

Thesis Advisors:

David S. Davis  
Richard C. Olsen

**Approved for public release; distribution is unlimited.**

<b>REPORT DOCUMENTATION PAGE</b>			Form Approved OMB No. 0704-0188	
Public reporting burden for this collection of information is estimated to average 1 hour per response, including the time for reviewing instruction, searching existing data sources, gathering and maintaining the data needed, and completing and reviewing the collection of information. Send comments regarding this burden estimate or any other aspect of this collection of information, including suggestions for reducing this burden, to Washington headquarters Services, Directorate for Information Operations and Reports, 1215 Jefferson Davis Highway, Suite 1204, Arlington, VA 22202-4302, and to the Office of Management and Budget, Paperwork Reduction Project (0704-0188) Washington DC 20503.				
1. AGENCY USE ONLY (Leave blank)		2. REPORT DATE December 1999		3. REPORT TYPE AND DATES COVERED Master's Thesis
4. TITLE AND SUBTITLE <b>OPERATION AND CALIBRATION OF THE NPS ULTRAVIOLET IMAGING SPECTROMETER (NUVIS) IN THE DETECTION OF SULFUR DIOXIDE PLUMES</b>				5. FUNDING NUMBERS
6. AUTHOR(S) Marino, Stephen A.				
7. PERFORMING ORGANIZATION NAME(S) AND ADDRESS(ES) Naval Postgraduate School Monterey, CA 93943-5000				8. PERFORMING ORGANIZATION REPORT NUMBER
9. SPONSORING / MONITORING AGENCY NAME(S) AND ADDRESS(ES) N/A				10. SPONSORING / MONITORING AGENCY REPORT NUMBER
11. SUPPLEMENTARY NOTES The views expressed in this thesis are those of the author and do not reflect the official policy or position of the Department of Defense or the U.S. Government.				
12a. DISTRIBUTION / AVAILABILITY STATEMENT Approved for public release; distribution is unlimited.				12b. DISTRIBUTION CODE: A
13. ABSTRACT (maximum 200 words)  The Naval Postgraduate School's Ultraviolet Imaging Spectrometer (NUVIS) is a hyperspectral sensor with a spectral response of 300 to 375 nanometers. This thesis research concentrates on the operation and calibration of NUVIS in the detection of effluent sulfur dioxide (SO <sub>2</sub> ) plumes. NUVIS is capable of detecting and quantifying SO <sub>2</sub> emissions in the form of effluent smokestack plumes by exploiting SO <sub>2</sub> 's unique UV absorption signature. Laboratory comparison UV spectra of SO <sub>2</sub> were recorded and used to calculate curves of growth for four different SO <sub>2</sub> spectral features. Laboratory results were employed to analyze field data taken of a coal-burning power plant. Analysis of this plume data yielded a mean plume SO <sub>2</sub> mixing ratio of 365 ± 200 ppm, in agreement with the <i>in situ</i> stack value of 400 ppm. Further assessment of NUVIS indicates that its lower limit for SO <sub>2</sub> detection in typical field applications is approximately 70 ppm.				
14. SUBJECT TERMS <b>Ultraviolet, Hyperspectral, Spectral Imaging, Spectrometer, Sulfur Dioxide, Pollution, Remote Sensing, Environmental Monitoring</b>				15. NUMBER OF PAGES 103
				16. PRICE CODE
17. SECURITY CLASSIFICATION OF REPORT Unclassified		18. SECURITY CLASSIFICATION OF THIS PAGE Unclassified		19. SECURITY CLASSIFICATION OF ABSTRACT Unclassified
				20. LIMITATION OF ABSTRACT UL

NSN 7540-01-280-5500

Standard Form 298 (Rev. 2-89)  
Prescribed by ANSI Std. Z39-18



**Approved for public release; distribution is unlimited**

**OPERATION AND CALIBRATION OF THE NPS ULTRAVIOLET IMAGING  
SPECTROMETER (NUVIS) IN THE DETECTION OF SULFUR DIOXIDE  
PLUMES**

Stephen A. Marino  
Lieutenant, United States Navy  
B.S., University of Pittsburgh, 1991

Submitted in partial fulfillment of the  
requirements for the degree of

**MASTER OF SCIENCE IN APPLIED PHYSICS**

from the

**NAVAL POSTGRADUATE SCHOOL  
December 1999**

Author: \_\_\_\_\_  
Stephen A. Marino

Approved by: \_\_\_\_\_  
David S. Davis, Thesis Advisor

\_\_\_\_\_  
Richard C. Olsen, Thesis Advisor

\_\_\_\_\_  
William B. Maier II, Chairman  
Department of Physics



## ABSTRACT

The Naval Postgraduate School's Ultraviolet Imaging Spectrometer (NUVIS) is a hyperspectral sensor with a spectral response of 300 to 375 nanometers. This thesis research concentrates on the operation and calibration of NUVIS in the detection of effluent sulfur dioxide (SO<sub>2</sub>) plumes. NUVIS is capable of detecting and quantifying SO<sub>2</sub> emissions in the form of effluent smokestack plumes by exploiting SO<sub>2</sub>'s unique UV absorption signature. Laboratory comparison UV spectra of SO<sub>2</sub> were recorded and used to calculate curves of growth for four different SO<sub>2</sub> spectral features. Laboratory results were employed to analyze field data taken of a coal-burning power plant. Analysis of this plume data yielded a mean plume SO<sub>2</sub> mixing ratio of  $365 \pm 200$  ppm, in agreement with the *in situ* stack value of 400 ppm. Further assessment of NUVIS indicates that its lower limit for SO<sub>2</sub> detection in typical field applications is approximately 70 ppm.



## TABLE OF CONTENTS

I. INTRODUCTION .....	1
A. MOTIVATION AND OBJECTIVES .....	1
B. OUTLINE .....	4
II. BACKGROUND.....	7
A. REMOTE SENSING AND SPECTRAL IMAGING .....	7
B. ULTRAVIOLET REMOTE SENSING.....	12
1. The Concept.....	12
2. Earth's Atmosphere and Ultraviolet Wavelengths.....	13
C. SULFUR DIOXIDE.....	15
1. An Atmospheric Pollutant .....	15
2. An Ultraviolet Absorber.....	18
D. ABSORPTION SPECTROSCOPY .....	20
1. Introduction.....	20
2. Terminology .....	22
3. The Curve of Growth.....	26
III. NUVIS.....	29
A. BACKGROUND.....	29
B. OPTICAL, OPTOMECHANICAL AND ELECTRONIC HARDWARE .....	29
C. THE COMPUTER, DATA ACQUISITION AND CONTROL SYSTEMS .....	32
D. DATA ACQUISITION, CONTROL AND DATA DISPLAY SOFTWARE.....	35
IV. LABORATORY CALIBRATIONS OF NUVIS.....	41
A. PURPOSE.....	41
B. WAVELENGTH CALIBRATION .....	41
C. EXPERIMENTAL OVERVIEW.....	43
D. LABORATORY MEASUREMENTS OF SO <sub>2</sub> .....	44
1. Gas Test Cells.....	45
2. Calibration Source and Reflective Screen.....	49
3. Test Cell Preparation .....	51
4. Data Acquisition.....	52
5. First Results.....	53
E. GENERATING EXPERIMENTAL CURVES OF GROWTH.....	55
1. Approach.....	55
2. Experimental Results .....	56
3. Analysis of Experimental Data .....	58
V. APPLICATION OF LABORATORY CALIBRATIONS TO FIELD DATA.....	63
A. FIELD EXPERIMENTS .....	63
B. RESULTS .....	67
VI. CONCLUSIONS AND RECOMMENDATIONS .....	75



APPENDIX A. NUVIS FIELD CHECKLIST .....	79
APPENDIX B. NUVIS OPERATIONAL CHECKLIST .....	81
APPENDIX C: RANGE EFFECTS AND NUVIS ANOMALIES .....	87
LIST OF REFERENCES .....	91
INITIAL DISTRIBUTION LIST .....	93

## **ACKNOWLEDGEMENTS**

The author would like to thank Dr. David Cleary whose enthusiasm was a major motivator in my decision to begin this work with NUVIS. Special thanks to Major Stephen Finney, USAF, for assisting in the 1999 field experiments and subsequent data analysis. Thanks to NPS staff members Jay Adeff and Don Snyder for their support during this research. Finally, the author would like to thank his wife, Michelle, for her love, devotion and patience.

## I. INTRODUCTION

### A. MOTIVATION AND OBJECTIVES

Remote sensing instruments are critical to the areas of technical intelligence, the remote sensing of hazards, and support to military operations. In an effort to enhance the capabilities available to the remote sensing community as well as to the military, we have pursued a little used portion of the electromagnetic spectrum. Over the last three years, we have designed and constructed an ultraviolet hyperspectral imager. Our motivation came, in part, from the success of the school's **Middle Ultraviolet SpecTrograph for Analysis of Nitrogen Gases (MUSTANG)**, a rocket-borne atmospheric research instrument. This resulted in the development of the **NPS UltraViolet Imaging Spectrometer (NUVIS)**, a hyperspectral imager that operates at near-ultraviolet wavelengths. NUVIS is one of the first such instruments of its kind: a portable, ground-based, hyperspectral imager that operates at ultraviolet (UV) wavelengths: nominally 300 to 375 nanometers (nm).

From the onset, NUVIS designers recognized that ultraviolet remote sensing could be used as an important tool in effluent analysis. Through the efforts of Dr. David Cleary, LT Todd Hooks and Major Andrew MacMannis, NUVIS was designed at the school, and fabrication of the instrument was completed in the fall of 1997. The next step was to focus research on the instrument's ability to analyze and characterize a chemical effluent plume. Such capabilities are of interest to both the civilian and military communities.

As initial testing was about to get underway, a major question arose: Could gaseous effluents emitted from smoke stacks be detected, imaged, identified, and quantified using hyperspectral remote sensing techniques at UV wavelengths? This thesis research set out to answer that question and to further define the instrument's capability to perform such a mission. In support of these efforts, the trace gas, sulfur dioxide (SO<sub>2</sub>), was targeted for study.

Numerous studies have focused on the topic of remote sensing of trace gases using spectroscopic monitoring techniques. Supporting literature indicates that considerable attention has been placed on the study and techniques of infrared remote sensing. Until now, remote sensing at ultraviolet wavelengths has received comparatively little attention. This study sets out to challenge such thinking by exploring new ways to exploit the ultraviolet region of the electromagnetic spectrum utilizing the recently developed technique of hyperspectral imaging.

Although ultraviolet wavelengths suffer more from atmospheric scattering and ozone absorption than do others, this study will show that NUVIS has already demonstrated dual-use imaging and spectroscopic capabilities and is capable of detecting, at short range, the effluent trace gas SO<sub>2</sub>. With this initial success, it became necessary to determine whether effluent SO<sub>2</sub> could reliably be identified, measured and quantized over longer distances using UV remote sensing. An approach was taken such that laboratory experiments, calibrations, and operational field testing would lead to an evaluation of NUVIS's capabilities to detect the trace gas and the utility of such technology.

This thesis project focuses on calibrating the spectrometer for the detection of gaseous sulfur dioxide. Laboratory experiments were conducted at known concentrations of SO<sub>2</sub> to measure changes in its absorption spectrum as a function of gas concentration. SO<sub>2</sub> is a triatomic molecule that has a set of strong absorption signatures between 300 and 325 nm. The detailed spectrum across this spectral region exhibits a number of identifiable absorption lines. For each observed line, an associated measure of its spectral absorption, called its equivalent width, may be easily measured. Calibration curves of the lines' equivalent widths versus gas concentration, called curves of growth, can then be generated.

During this research, six sets of calibration data were analyzed. From this analysis, four individual absorption lines were identified for equivalent width measurements. Four curves of growth were successfully generated from these laboratory experiments. These calibration curves were then applied to field data in an initial attempt to quantify effluent SO<sub>2</sub> concentrations.

It should be noted that my involvement with NUVIS came at a time when nearly all of the instrument's initial designers had either moved on from the school or were in the process of leaving. Because of this, a period existed where Dr. Cleary had done a considerable amount of work with the instrument himself, and the majority of this work had gone unpublished. Because Hooks and MacMannis were unable to complete laboratory and field testing of the instrument, a detailed operating procedure had not yet been developed. This thesis will not only present the work involved with generating the

SO<sub>2</sub> curves of growth but will also outline the basic operating procedures for the instrument. Such documentation had not existed prior to this study.

In an attempt to maintain continuity with the work done by Hooks and MacMannis, this thesis also includes certain portions of Dr. Cleary's unpublished work as background material. This is in part due to the fact that the current NUVIS system has undergone certain improvements from its original configuration. Where appropriate, the inclusion of such material is clearly indicated.

In 1998, ground-based field experiments were conducted and resulted in preliminary spectroscopy and spectral imagery of effluent SO<sub>2</sub>-producing targets. This thesis research, the accompanying calibration, a follow-on field experiment, and the resultant data analysis have all been accomplished in support of chemical plume detection, analysis and characterization with respect to sulfur dioxide. The work involved in this study is a follow-on to the initial experimental research initiated in 1998.

## **B. OUTLINE**

This thesis is divided into six chapters and three appendices. Chapter II provides the necessary background material on the topics of remote sensing and hyperspectral imaging, ultraviolet remote sensing, sulfur dioxide and absorption spectroscopy. The NUVIS instrument will be presented in Chapter III. Chapter IV details the laboratory calibration of NUVIS and includes resultant curves of growth, one for each of the four SO<sub>2</sub> absorption lines selected for analysis. Field data is briefly analyzed by a simple application of these laboratory calibrations developed in Chapter IV. This process and

the accompanying results are presented in Chapter V. Conclusions and recommendations are contained in Chapter VI. Appendix A provides a recommended checklist for NUVIS field operation. Appendix B briefly details the system operating procedure. Appendix C provides additional data that should be considered in future reasearch.

THIS PAGE INTENTIONALLY LEFT BLANK



## II. BACKGROUND

### A. REMOTE SENSING AND SPECTRAL IMAGING

Remote sensing is a generic term used to describe all of the measurements made at a distance from an object to be observed. It involves collecting information about an object without being in direct contact with that object. Typically the information being collected is carried by electromagnetic waves, although other means are sometimes used. If the source of these waves is a man-made emitter, then the process is dubbed active remote sensing. If the source of these waves is natural, the process is known as passive remote sensing (Lenoble, 1993). It is passive remote sensing at near-ultraviolet wavelengths (200-400nm) with which NUVIS is most concerned. As a quick reference, Table 2.1 lists some typical wavelength, frequency and wavenumber ranges for various regions of the electromagnetic spectrum.

Name	Wavelengths (nm)	Frequencies (Hz)	Wavenumbers (cm <sup>-1</sup> )
Radio	$\sim 10^8$ - $10^{13}$	$\sim 3 \times 10^4$ - $3 \times 10^9$	$10^{-6}$ -0.1
Microwave	$\sim 10^7$ - $10^8$	$\sim 3 \times 10^9$ - $3 \times 10^{10}$	0.1-1
Infrared	$\sim 10^3$ - $10^7$	$\sim 3 \times 10^{10}$ - $3 \times 10^{14}$	1- $10^4$
Visible	700-400	$\sim (4.3$ - $7.1) \times 10^{14}$	$(1.4$ - $2.4) \times 10^4$
Ultraviolet	$\sim 400$ -50	$\sim 7.5 \times 10^{14}$ - $6.0 \times 10^{15}$	$(2.5$ - $20) \times 10^4$
X Ray	$\sim 50$ -0.1	$\sim (0.6$ - $300) \times 10^{16}$	$(0.2$ - $100) \times 10^6$
Gamma Ray	$\leq 0.1$	To $3 \times 10^{18}$	$\geq 10^8$

Table 2. 1. Typical wavelengths, frequencies and wavenumbers for various regions of the electromagnetic spectrum.

Over the last decade, a number of instrument platforms have been developed for the express purpose of optical remote sensing. These platforms have been employed in a number of field operations, ranging from space-based and air-based missions to ground-based applications. Spectral imagers are one such instrument family, and they have quickly become workhorses of the remote sensing community. Spectral imagers measure both the 2-D image produced by a scene and the spectral content of each picture element (pixel) of the image. These spectral imagers are classified by the width of the spectral bands they record. Figure 2.1 provides a brief overview of such classifications.

The motivation behind the development of NUVIS was a perceived need to explore the near-UV wavelength region with an operational hyperspectral imager. Such an instrument would be capable of collecting data from tens to hundreds of bands at a much smaller bandwidth resolution than that of a conventional multispectral sensor.

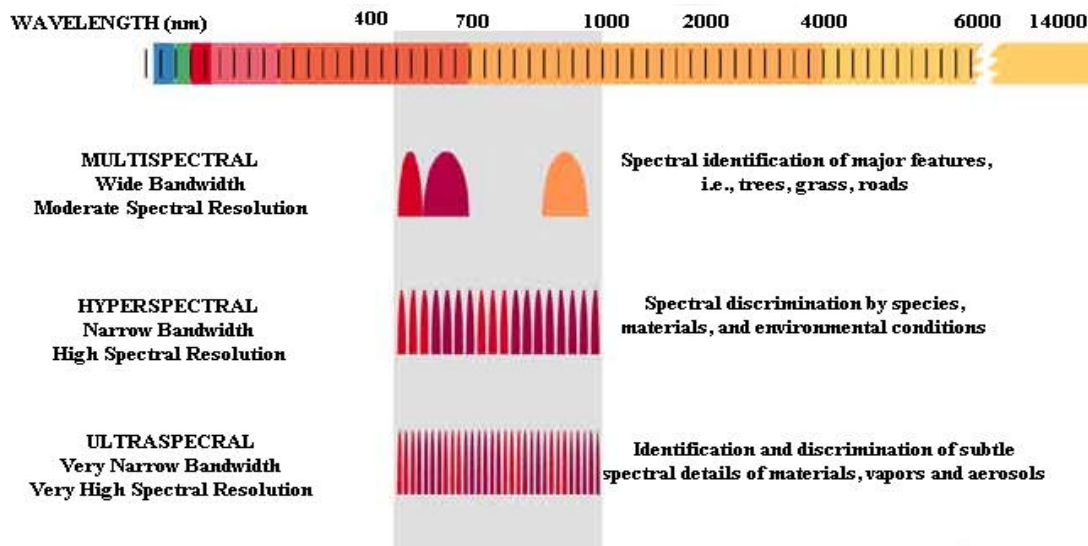


Figure 2. 1. Spectral imager classifications. From Multispectral Users Guide, 1995.

Related research that began in 1996 resulted in the NUVIS instrument of today, a hyperspectral imager with a spectral bandwidth of 300 to 375 nm at a resolution of approximately 0.3 nm. (Cleary, 1998)

A hyperspectral imager produces a spectral image of a scene, which is typically displayed in a format known as a hyperspectral cube. Imaging spectrometers typically use a two-dimensional array (e.g., a CCD) and produce the three-dimensional data cube containing two spatial dimensions and a third spectral dimension. The third dimension is obtained by scanning either the spectral dimension or one of the two spatial dimensions. NUVIS is the latter type. A sample of NUVIS output is demonstrated in the image cube illustrated in Figure 2.2. A large number of images are created from contiguous, rather than disjoint regions of the spectrum. This technique typically yields finer resolution than is possible with a multispectral imager and in doing so, provides much more information to the data analyst. It is from this series of images, each measuring the level of incident energy at a specific wavelength, that a combined image is formed.

Today, countless airborne hyperspectral sensors are employed in the field. Table 2.2 provides a summary of many of these instruments. This table also demonstrates the relative non-existence of UV hyperspectral imagers. Thus, NUVIS is a portable, ground based, passive remote sensor capable of hyperspectral imaging at UV wavelengths; a prototype instrument that could someday possibly be employed as an airborne sensor.

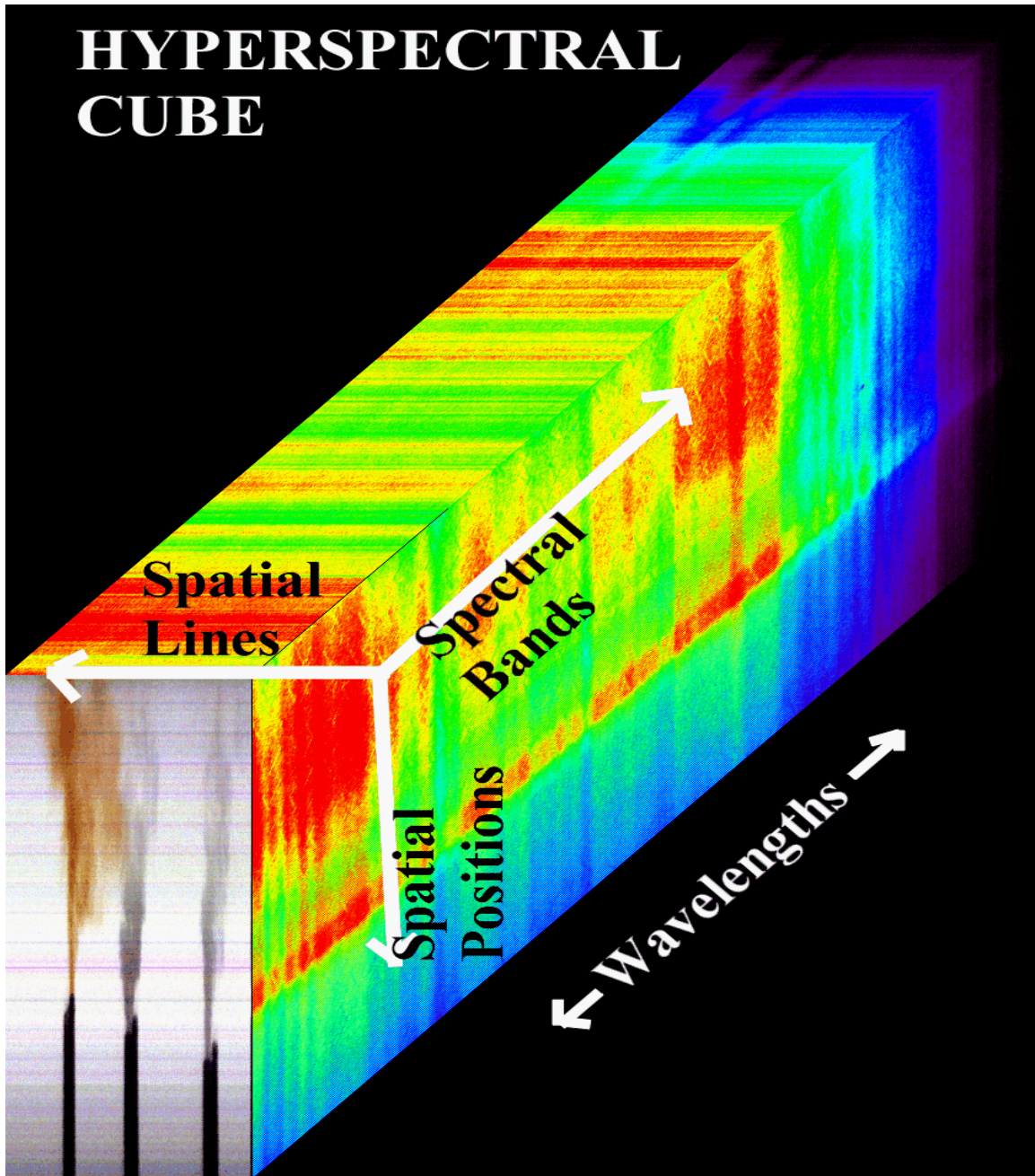


Figure 2. 2. NUVIS hyperspectral cube. Image illustrates the two spatial and one spectral dimension comprising the image cube.

Sensor (Agency)	Number of Bands	Spectral Range(nm)	Bandwidth FWHM(nm)	IFOV (mrad)	FOV (deg)	Data	Period of Operation
AAS (ASTER) (DAIS-2815) (GER)	1 3 20	760-850 3000-5000 8000-12000	90 600-700 200	1.0,2.5, or 5.0	28.8,65 , or 104	Image Cube (IC)	Since(s) 1991
AHS, Daedalus	48	440-12700	20-1500	2.5	86	IC	1994
AIS-1	128	990-2100 1200-2400	9.3	1.91	3.7	IC	1982-85
AIS-2 (NASA/JPL)	128	800-1600 1200-2400	10.6	2.05	7.3	IC	1986-87
AISA (Karelsilva Oy)	1-286	450-900	1.56-9.36	1	21	IC	S1993
AMSS (Geoscan)	32 8 6	490-1090 2020-8500- 12K	170-240 430-440 550-590	2.1x3.0	92	IC	S1985
Sensor (Agency)	Number of Bands	Spectral Range(nm)	Bandwidth at FWHM (nm)	IFOV (mrad)	FOV (deg)	Data	Period of Operation
ARES (AIP)	75	2000-6300	25-70	1.17	3x3	IC	S1985
ASAS Upgraded ASAS (NASA/GSFC)	29 62	455-873 400-1060	15 11.5	0.80 0.80	25 25	IC	1987-91 S1991
AVIRIS (JPL)	224	380-2500	9.7-12.0	1	30	IC	S1987
CASI (Itres Research)	288 19	400-1000 nominal	650	1.3,1.6	37.8 44.7	Profile Image	S1990
CIS (China)	64 24 1 2	400-1040 2000-2480 3530-3940 10.5K-12.5K	10 20 410 1000	1.2x3.6 1.2x1.8 1.2x1.2 1.2x1.2	80deg	IC	S1993
CHRIS, SAIC AHIS, (SAIC)	40 288	430-860 440-880	11 3	0.05 1.0	10 11.5	IC IC	1992 1994
DAIS-7915 (GER/DLR)	32 8 32 1 6	400-1010 1500-1780 1970-2450 3000-5000 8.7K-12.7K	10-16 36 36 2000 600	3.3,2.5, or 5.0	64-78	IC	S1994
DAIS-16115 (GER)	76 32 32 6 12 2	400-1000 1000-1800 2000-2500 3000-5000 8K-12K 400-1000	8 25 16 333 333 stereo	3	78	IC	S1994
DAIS-3715 (GER)	32 1 2 1 1	360-1000 1000-2000 2175-2350 3000-5000 8K-12K	20 1000 50 2000 4000	5	±45	IC	S1994
FLI/PMI (Moniteq)	≥288	430-805	2.5	1.3	70	Profile Image	1984-90
FTVHSI (Kestrel)	256	440-1150	67cm <sup>-1</sup>	0.8	15	IC	1996
GER-63 Channel Scanner (GER)	24 4 29 6	400-1000 1500-2000 2000-2500 8K-12.5K	25 125 17.2 750	2.5,3.3, or 4.5	90	IC	S1986
Continued on next page.							

Sensor (Agency)	Number of Bands	Spectral Range(nm)	BandwidthF WHM(nm)	IFOV (mrad)	FOV (deg)	Data	Period of Operation
HYDICE (NRL/ERIM)	206	400-2500	7.6-14.9	0.5	8.94	IC	1994
ISM (DESPA/IAS/OPS)	64 64	800-1600 1600-3200	12.5 25.0	3.3x11.7	40	IC	S1991
MAS (Daedalus)	50	547-14.5K	31-517	2.5	85.92	IC	S1992
MISI(RIT)	60	400-1000	10	2	±45	IC	S1996
MIVIS (Daedalus)	20 8 64 10	433-833 1150-1550 2000-2500 8.2K-12.7K	20 50 8 400-500	2.0	70	IC	1993
MUSIC (Lockheed)	90 90	2500-7000 6K-14.5K	25-70 60-1400	0.5	1.3	IC	1989
ROSIS (MBB/ DLR/GKSS)	84	430-830 (≤2400)	4-12	0.56	16 (32)	IC	S1993
SFSI (CCRS)	115	1200-2400	10.4	0.4	9.4	IC	S1994
SMIFTS (U. of Hawaii)	75 35	1000-5200 3200-5200	100cm <sup>-1</sup> 50cm <sup>-1</sup>	0.6	6.0	IC	S1993
TRWIS-A	128	430-850	3.3	1.0	15	IC	1990
TRWIS-B	90	460-880	4.8	1.0	15	IC	1991
TRWIS-II	80	1500-2500	12	0.5/1.0	7.5/15	IC	1992
TRWIS-III (TRW)	384	300-2500	5/6.25	0.9	15	IC IC	1995
Hybrid VIFIS (U. of Dundee)	30 30	440-640 620-890	10-14 14-18	1 1	31.5 31.5	IC	Test1994
WIS-FDU WIS-VNIR WIS-SWIR (Hughes SRBC)	64 129,265 81+90	400-1030 400-1000 1000-2500		1.36 0.66 0.66	10&15 19.1 12.0	IC IC IC	Test1992 1995 1995

Table 2. 2. Summary of hyperspectral airborne imaging spectrometers.

From Kramer,1996.

## B. ULTRAVIOLET REMOTE SENSING

### 1. The Concept

Passive remote sensing at ultraviolet wavelengths is quite dependent on the spectral distribution of the solar irradiance at ground level. This distribution is illustrated in Figure 2.3. From this diagram, it is easy to see that the solar irradiance available at ultraviolet wavelengths is relatively low compared to that at visible and infrared wavelengths. NUVIS was designed to operate in the daytime, using ambient scattered UV radiation in the 300 to 400nm spectral band.

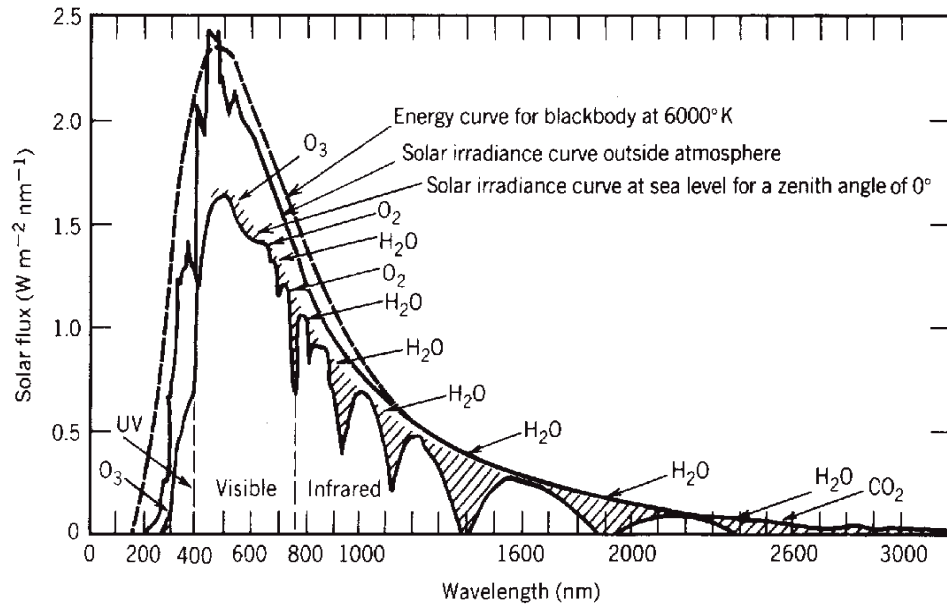


Figure 2. 3. Spectral distribution of the solar irradiance (flux). Notice that the magnitude of the available flux falls off rapidly below 400nm. This decline is due, in part, to ozone absorption, which will be discussed later. From Finlayson-Pitts & Pitts, 1986.

## 2. Earth's Atmosphere and Ultraviolet Wavelengths

The earth's atmosphere can be divided into a number of atmospheric layers each with its own unique characteristics. Figure 2.4 illustrates these layers and provides the approximate behavior of temperature over these regions. One distinguishing characteristic of the earth's atmosphere is that it is generally a homogeneous mixture of nonreactive major component gases ( $N_2$ ,  $O_2$ , noble gases) superimposed upon variable concentrations of minor volatile and/or chemically reactive gases, as indicated in Table 2.3.

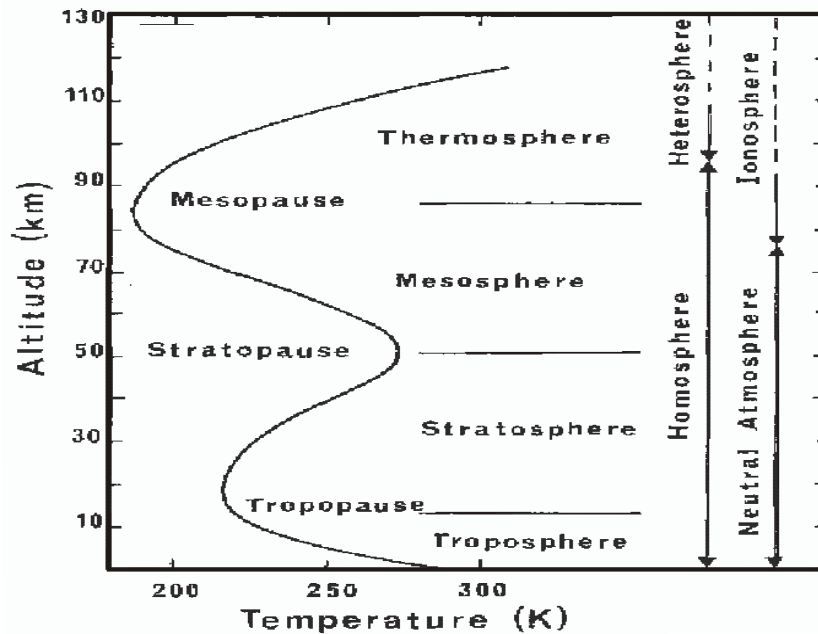


Figure 2. 4. Atmospheric layers. From Lenoble, 1993.

Constituent Name / (type)	Formula	Molec. Mass	% by volume
Nitrogen/ (Permanent)	N <sub>2</sub>	28.0134	78.084
Oxygen / (Permanent)	O <sub>2</sub>	31.9988	20.9476
Argon / (Permanent)	Ar	39.948	0.934
Water Vapor / (Variable)	H <sub>2</sub> O	18.0160	0-7
Carbon Dioxide / (Variable)	CO <sub>2</sub>	44.00995	0.01-0.1
Ozone / (Variable)	O <sub>3</sub>	47.9982	0-0.01
Neon / (Permanent)	Ne	20.183	0.001818
Helium / (Permanent)	He	4.0026	0.000524
Methane / (Permanent)	CH <sub>4</sub>	16.04303	0.0002
Sulfur Dioxide / (Variable)	SO <sub>2</sub>	64.064	0-0.0001
Hydrogen / (Permanent)	H <sub>2</sub>	2.01594	0.00005
Nitrogen Dioxide / (Variable)	NO <sub>2</sub>	46.0055	0-0.000002

Table 2. 3. Atmospheric constituents. From Durkee, 1999.

Since NUVIS currently operates at ground level, the properties of ultraviolet radiation in the lower troposphere are of paramount interest. Before any solar ultraviolet radiation can reach the troposphere, it must first pass through the various overlying



atmospheric layers. Far ultraviolet wavelengths are strongly absorbed at higher altitudes (above 100km) by molecular and atomic oxygen and nitrogen. More importantly, a great majority of UV absorption is caused by oxygen in the mesosphere and upper stratosphere, principally in the form of ozone. These absorbers are active in the spectral bandpass of NUVIS (~300nm). Figure 2.5 summarizes these effects.

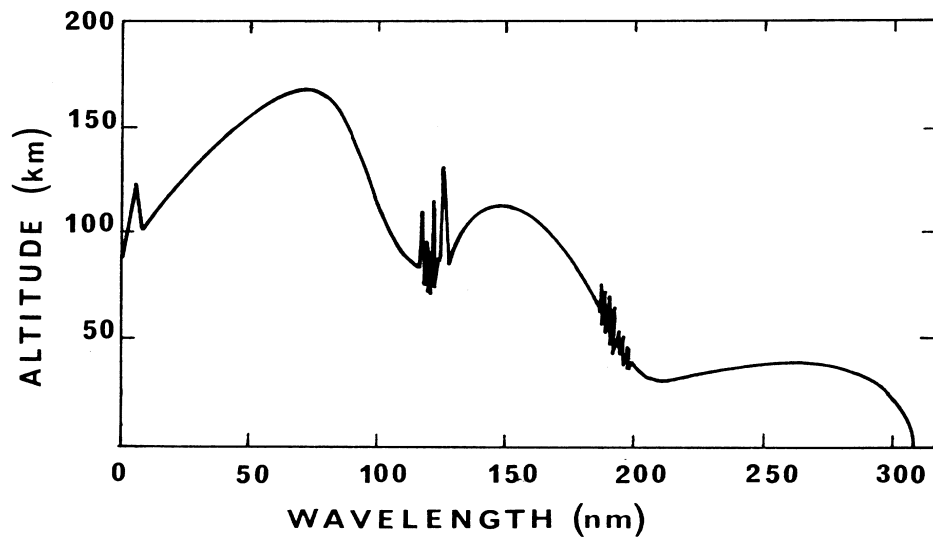


Figure 2. 5. Depth of penetration of solar radiation. Altitudes correspond to an attenuation of  $1/e$ . From Lenoble, 1993.

## C. SULFUR DIOXIDE

### 1. An Atmospheric Pollutant

Absorption of ultraviolet radiation by atmospheric gases is not limited to the cases of nitrogen, oxygen and ozone alone. There are a number of trace gases in the atmosphere that absorb at these shorter (UV) wavelengths. Nitrogen dioxide ( $\text{NO}_2$ )

and sulfur dioxide ( $\text{SO}_2$ ) are two such examples. For the purpose of this work, only the trace gas, sulfur dioxide, will be studied.

Sulfur dioxide, Figure 2.6, is a colorless gas, which has a characteristic suffocating odor. It is extremely irritating to the eyes and respiratory tract. It is formed in the combustion of sulfur-containing fuels and in the smelting of sulfide ores and is a major atmospheric pollutant. This trace gas is only a small part of the much larger sulfur cycle illustrated in Figure 2.7. This cycle not only demonstrates that  $\text{SO}_2$  is a primary pollutant emitted by fuel combustion (from coal burning power plants) but also demonstrates that most volcanic sulfur is emitted as  $\text{SO}_2$  (Finlayson-Pitts and Pitts, 1986).

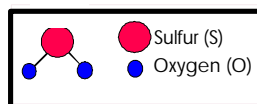


Figure 2. 6. Sulfur dioxide molecule ( $\text{SO}_2$ ) .

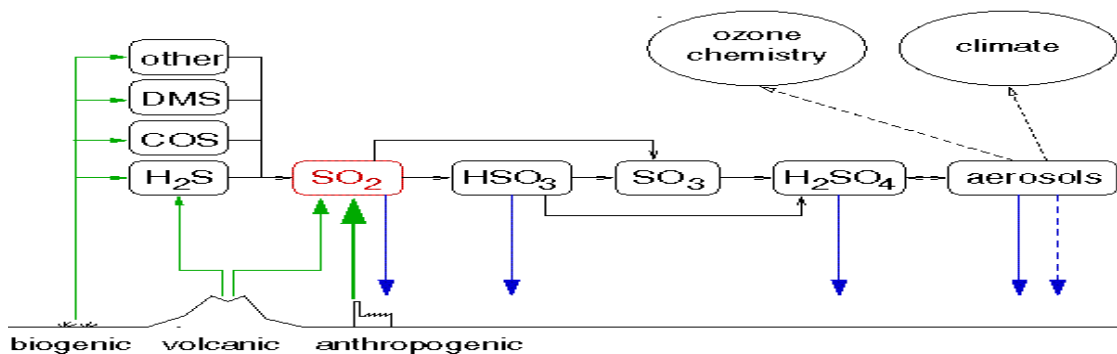


Figure 2. 7. Sulfur cycle demonstrating volcanic and man-made sources of  $\text{SO}_2$ .

Monitoring of sulfur dioxide has become a global concern as data are routinely collected from a number of different sensors to monitor SO<sub>2</sub> levels worldwide. Monitoring SO<sub>2</sub> is of interest for a number of reasons. In regions of high volcanic activity, SO<sub>2</sub> monitoring can provide yet another valuable tool to assist in the study of volcanic activity. For years now, the Correlating Spectrometer (COSPEC), a non-imaging spectrometer, has been employed by vulcanologists to monitor effluent SO<sub>2</sub> levels ( see Figure 2.8 ). Such monitoring is important, especially in densely populated regions, to aid in predicting volcanic activity and to warn of a rise in SO<sub>2</sub> concentrations at ground level.



Figure 2. 8. COSPEC instrument at a volcanic site. From USGS, 1999.

The Environmental Protection Agency (EPA) has long been interested in monitoring anthropogenic (man-made) sources of sulfur dioxide. A primary focus has been placed on coal burning power plants. The EPA has established strict guidelines for allowable types and levels of emissions that these plants can produce. Monitoring effluent levels from these sources can be accomplished either by sensors installed within the power plant's stacks themselves (*in situ* measurements) or by remote sensing techniques.

With these factors in mind, NUVIS designers set out to build an instrument capable of detecting SO<sub>2</sub> emissions from both natural and man-made effluent sources. Since typical SO<sub>2</sub> concentrations range from only tens of ppm in the case of regulated power plants to hundreds or even thousands of ppm for volcanic vents, NUVIS would be required to detect SO<sub>2</sub> over a very wide range of absorption column densities.

## **2. An Ultraviolet Absorber**

Sulfur dioxide was chosen for study because the gas exhibits a strong absorption signature in the near-ultraviolet (200-400nm). This signature is illustrated in Figure 2.9. Although SO<sub>2</sub> absorbs to some extent over the entire 240 to 320nm wavelength range, the region longward of 300nm is of most interest for measuring SO<sub>2</sub> concentrations in the atmosphere. This region is advantageous because the illumination source for doing absorption spectroscopy in the field is Rayleigh scattered solar UV radiation. At ground level, this scattered radiation diminishes sharply at wavelengths shorter than about 300nm (see Figure 2.3). A further advantage is that in this region, SO<sub>2</sub> spectra can be

readily distinguished from the spectra of other absorbers (see Figure 2.10). Hence, we chose to concentrate on laboratory and field measurements of SO<sub>2</sub> spectra in the 300 to 350 nm wavelength range.

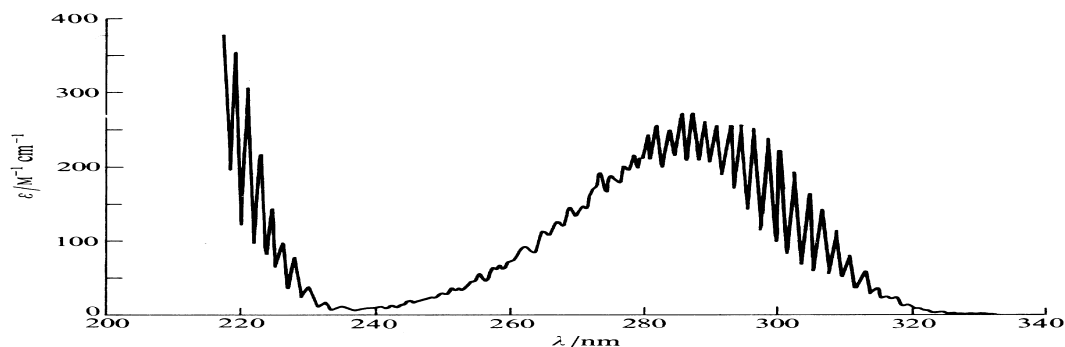


Figure 2. 9. Gas phase absorption spectrum of SO<sub>2</sub>. The extinction coefficient  $\epsilon$  is proportional to the absorptivity coefficient presented in section I.D.2. From Atkins, 1990.

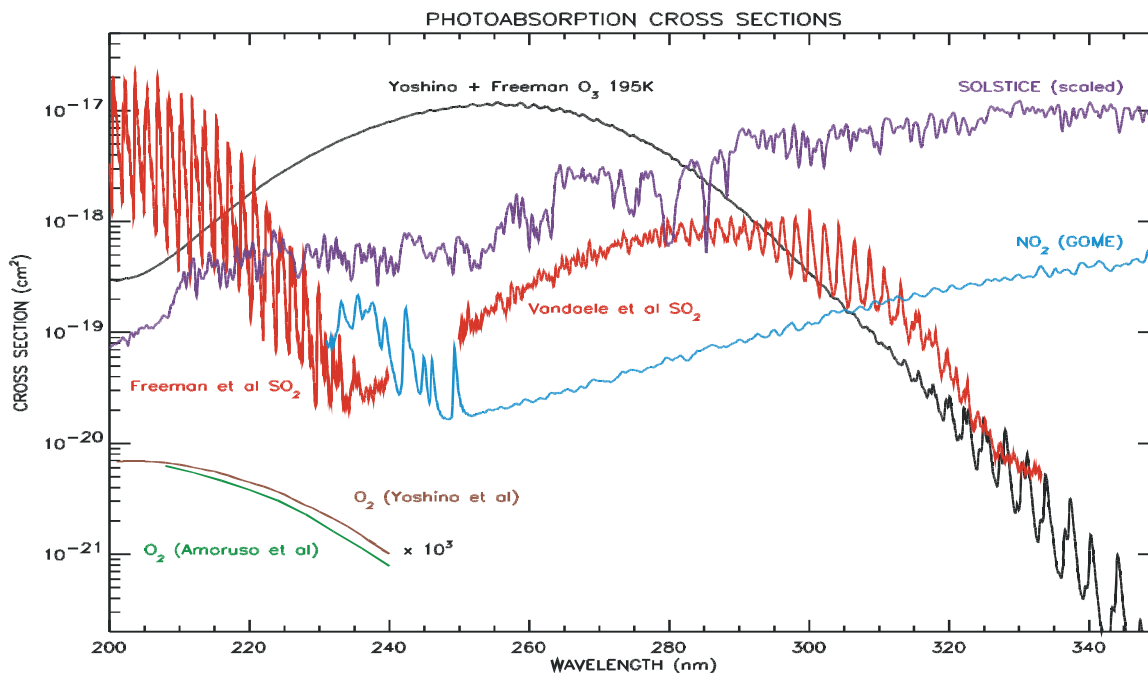


Figure 2. 10. Photoabsorption cross sections of atmospheric UV absorbers. Solar UV cross section data obtained from the Solar Stellar Irradiance Comparison Experiment (SOLSTICE) is also displayed. From Strickland, 1999.

## D. ABSORPTION SPECTROSCOPY

### 1. Introduction

Absorption spectroscopy is the study of the wavelength-dependent absorption of radiation from a continuum source by some chemical species of interest. In the laboratory, this technique usually involves working with a calibrated continuum light source. In NUVIS field applications, the background continuum source is the ambient Rayleigh scattered UV solar radiation, as discussed above.

The solar irradiance striking the atmosphere has approximately the spectral distribution of a 5800 K blackbody (see Figure 2.3). The Raleigh scattering cross section is proportional to  $1/\lambda^4$ , where  $\lambda$  denotes wavelength (Lenoble, 1993). The combined effect of these two natural phenomena is to provide a useful background continuum source in the 300nm wavelength region. The COSPEC instrument previously mentioned also utilizes this continuum radiation source.

Understanding how molecular absorption spectroscopy is used to measure molecular concentrations requires a basic knowledge of the energetics of the molecules of interest. The total energy  $E$  of a molecule arises from four contributions, represented by the following equation:

$$E = E_{\text{rot}} + E_{\text{vib}} + E_{\text{elec}} + E_{\text{trans}} . \quad (2-1)$$

$E_{\text{rot}}$  is the rotational energy of the free molecule about its center of mass.  $E_{\text{vib}}$  is the vibrational energy of the constituent atoms, typically in one of the molecule's vibrational normal modes.  $E_{\text{elec}}$  is the electronic energy analogous to that of the electronic energy of

isolated atoms.  $E_{\text{trans}}$  is the molecule's overall translational kinetic energy. In spectroscopic applications, the rotational, vibrational and electronic energy levels are of interest, since energy is quantized for these modes of free atoms and molecules. Because of the bond energies, masses and moments of inertia of small molecules, transitions between rotational states are usually observed at infrared and longer wavelengths. Vibrational transitions are typically observed at visible and infrared wavelengths. Electronic transitions generally occur at visible and UV wavelengths. (Lenoble, 1993)

Figure 2.11 provides a generalized representation of these energy levels for a simple molecule. Like many other molecules, gaseous  $\text{SO}_2$  exhibits its own unique characteristic UV absorption spectrum. If an incident radiation field induces photons

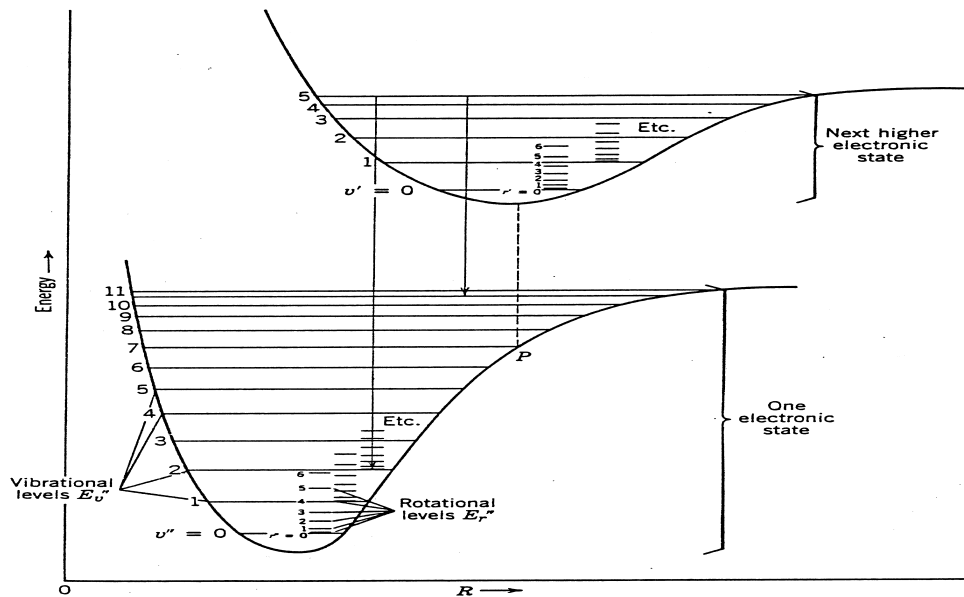


Figure 2. 11. Molecular energy curves for two electronic states. These curves demonstrate the relationship between vibrational, rotational and electronic levels. (This general depiction is not to scale.) From Eisberg and Resnick, 1985.

whose energies correspond to the difference between two energy levels of the molecule, the molecule may absorb a photon and jump to a higher energy level. The result is a wavelength-dependent absorption, or absorption spectrum, that is characteristic of the quantum structure of the absorbing species.

## 2. Terminology

Transmittance is the term used to describe the fraction of the energy of the incident radiation that passes through an absorbing medium. Figure 2.12 illustrates a beam of parallel radiation before and after it has passed through a layer of absorbing medium having a thickness of  $d$  and a concentration of  $c$  of an absorbing species. Due to the interactions between the incident photons and the absorbing particles, an incident intensity  $I_0$  is attenuated to an exiting intensity  $I$  (Skoog, 1985). The transmittance  $T$  of

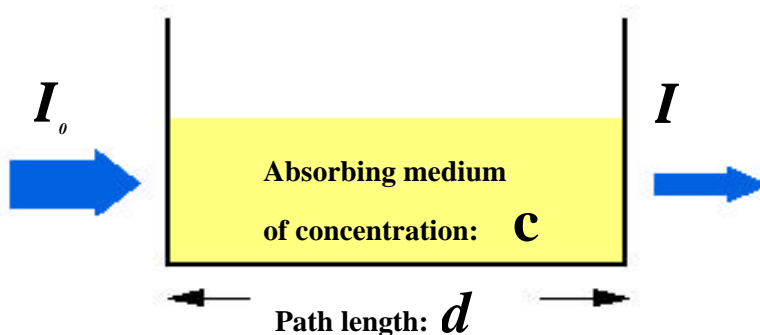


Figure 2. 12. A parallel beam of incident radiation before and after it has passed through a layer of absorbing medium.

the medium is thus defined as the ratio

$$T = I / I_0. \quad (2.2)$$



Absorbance,  $A$  is defined as

$$A = -\log(T) = \log(I_0 / I). \quad (2.3)$$

If the likelihood of multiple absorptions and reemissions along the path is small, there is a linear relationship between absorbance and concentration of an absorbing species given by Beer's Law

$$A = a(l) d c \quad (2.4)$$

(Skoog, 1985). The function  $a(l)$  is called the absorptivity coefficient. From Beer's Law, the attenuation of a signal can be given by

$$I = I_0 \exp(-s N d), \quad (2.5)$$

where  $s$  is the absorption cross section and  $N$  is the molecular number density.

Absorption is a quantity that differs from absorbance. It can be described in terms of the Einstein probability coefficient,  $B_{12}$ , but in practice, it is more often described in terms of an absorption coefficient,  $k(n)$ . This parameter describes the fractional decrease in flux density (intensity) at frequency  $n$  per unit path length through the absorbing medium:

$$-dI(n) = I(n) k(n) dx, \quad (2.6)$$

where  $I(n)$  is incident upon the layer of thickness  $dx$ . Assuming a homogeneous layer of thickness  $d$ , integration yields

$$I_d(n) = I_0(n) \exp(-k(n) d), \quad (2.7)$$

where  $k(n) d$  is known as the frequency-dependent optical depth,  $t(n)$ . The effect of increasing optical depth on an isolated absorption line profile is illustrated in Figure 2.13. (Thorne et al., 1999)

From a practical standpoint, it is the effective area of an absorption line that gives the most useful measure of spectral absorption that is taking place. The areas under the absorption lines (curves) of Figure 2.13, may be defined by the following equation,

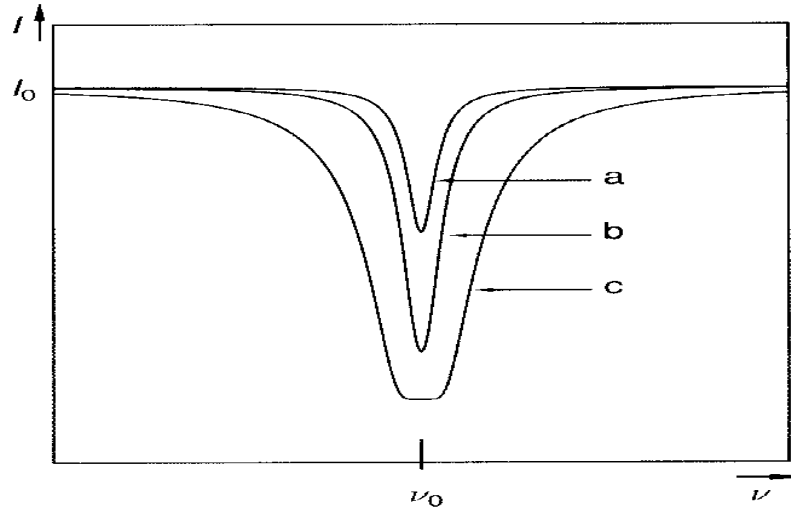


Figure 2. 13. Hypothetical absorption line profiles demonstrating the effect that an increase in optical depth has on a line shape. Lines a, b, and c represent shapes for increasing optical depths,  $t(n)$  . From Thorne et. al., 1999.

which is normalized to the incident flux density,

$$W = \hat{q}_{ine} (1 - \exp[-k(n)]) dn. \quad (2.8)$$

Equation 2.8 equates well to transmittance through the following relation,

$$W = \int_{\nu_{inc}} [1 - T(n)] d\nu, \quad (2.9)$$

where  $W$  is called the line's equivalent width, and  $T(n)$  is the frequency dependent transmittance from equation 2.2. Figure 2.14 further depicts the equivalent width of spectral line where the shaded area is equivalent to the area between the line profile and the continuum baseline,  $I(0)$ .

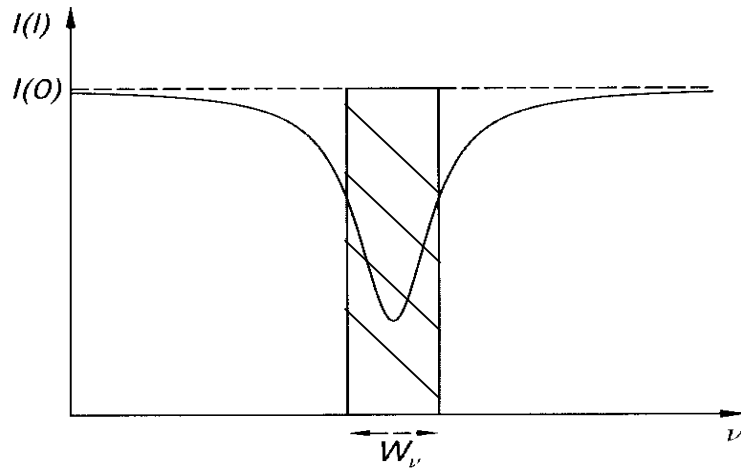


Figure 2. 14. Equivalent width measurement. Note that the shaded area is equal to the area between the line profile and continuum baseline,  $I(0)$ . From Thorne et. al., 1999.

It should be noted that the actual absorption of an isolated spectral line can be spread over a broad range of frequencies by natural, Doppler and pressure broadening (Thorne et al., 1999). Furthermore, the relation between the absorbance and  $I(n)$  is logarithmic, not linear, so equation 2.9 does not hold true for all cases. Measuring individual equivalent line widths is thus a more detailed process than measuring the overall trend of the absorption cross section of Equation 2.5. However, it can be shown

that linearity applies as long as the absorbing line is not highly saturated (  $I(\mathbf{n}) \approx 0$  at the profile's center ). Therefore, for the purposes of this thesis research, Equation 2.9 was utilized in calculating equivalent widths using nonsaturated lines. This was accomplished without correcting for any line shape effects and assumed that Equation 2.9 was applicable to all equivalent width measurements. For a more detailed approach, see Thorne et. al, 1999.

### 3. The Curve of Growth

In spectrochemical analysis by means of absorption spectroscopy, it has become standard practice to quantify the effects of an absorbing species abundance on the profile of an absorption line as an empirical graph called a curve of growth. The curve of growth for a spectral line describes the behavior of the equivalent width as a function of concentration of the absorbing species. It normally takes the form of a log-log plot as illustrated in Figure 2.15. In practice, the equivalent widths are measured for a series of known absorber concentrations in the laboratory. The equivalent width of lines found in

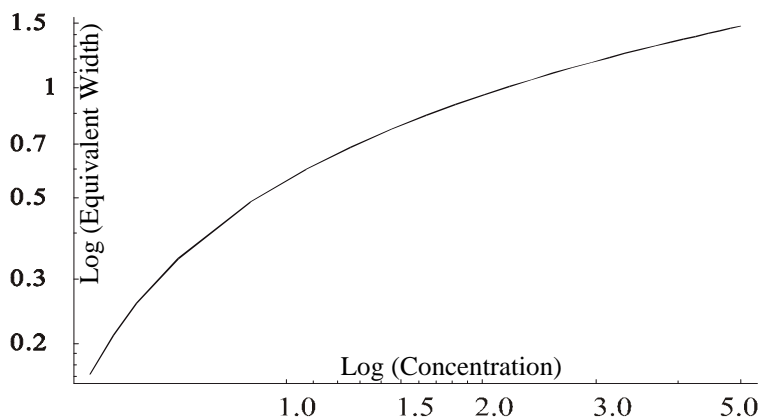


Figure 2. 15. Typical curve of growth. (Also known as a calibration curve.)

field data may be subsequently compared to the curve of growth, which then yields the molecular abundance of the field sample.

Remarkably, curve of growth analysis has been found to be relatively insensitive to different line profile shapes (Thorne et. al., 1999). Hence, it is of general utility across a wide variety of spectroscopic instruments and conditions. Two commonly encountered line shapes, Gaussian and Lorentzian, are illustrated in Figure 2.16. This study will only

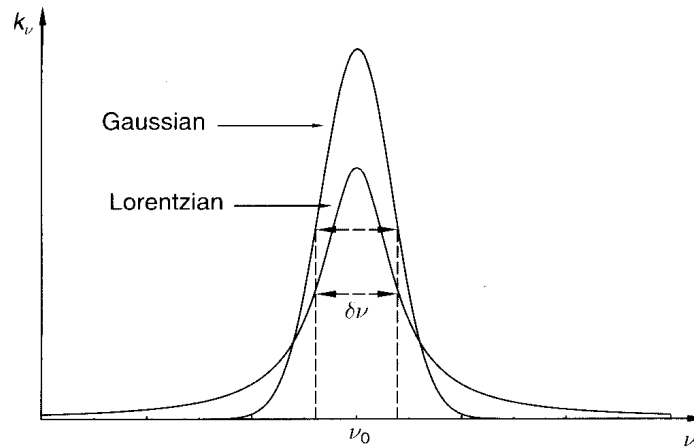


Figure 2. 16. Gaussian and Lorentzian profiles. Areas under each curve are the same.  
From Thorn et.al., 1999.

involve calculations based on Gaussian line profiles that may be represented by curves having the generalized form:

$$F(x)=A_0 \exp\{-(x- A_1)/ A_2\}^2/2\}, \quad (2.10)$$

where  $F(x)$  is the profile,  $A_0$  is the height of the Gaussian,  $A_1$  is the center of the Gaussian and  $A_2$  is the width of the Gaussian. Equation 2.10 will be utilized in the curve of growth calibration of the NUVIS instrument and in the analysis of field data presented in Chapters IV and V.

### **III. NUVIS**

#### **A. BACKGROUND**

NUVIS was designed, developed and constructed by former NPS Associate Professor Dr. David Cleary and students, Todd Hooks (Hooks, 1997) and Andrew MacMannis (MacMannis, 1997). It is the latest in a succession of ultraviolet spectroscopic instruments developed by Dr. Cleary and is the first to incorporate spectral imaging capabilities (Cleary, 1998). For a more detailed account of some of this earlier work done on UV instruments such as MUSTANG and DUUVIS, see Johnson, 1996.

#### **B. OPTICAL, OPTOMECHANICAL AND ELECTRONIC HARDWARE**

In principle, the NUVIS instrument of today is identical to the instrument first developed by Hooks and MacMannis. Designed and built to test the utility of hyperspectral imaging at ultraviolet wavelengths, the instrument's optical design is a classic Rowland circle spectrograph and its imaging design follows that of a push broom scanner. As it appears in Figure 3.1, NUVIS is a portable instrument capable of field operation with ease. Instrumental parameters remain as originally detailed by Dr. Cleary and are summarized in Table 3.1.

The instrument itself is comprised of nine basic components, which are illustrated in Figure 3.2. Light enters the instrument through a filter window, designed to pass only UV wavelengths. It then encounters a scanning mirror assembly. This assembly is comprised of three sub-components: 1) the mirror itself, 2) a stepper motor driver, which

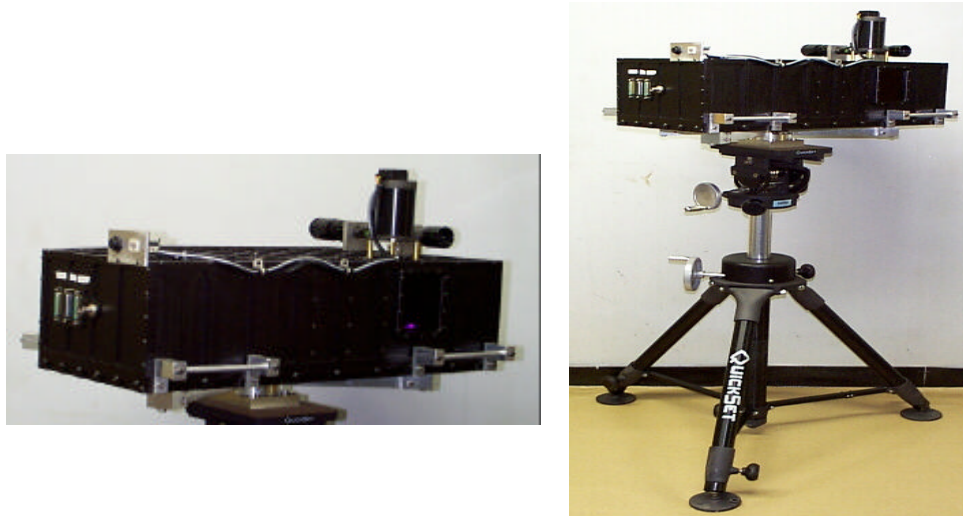


Figure 3.1. NUVIS instrument.

NUVIS PARAMETERS	
Optical Design	Rowland Circle Spectrograph
Imaging Design	Push Broom Scanner
Spectral Response	300 to 375nm
Spectral Resolution	0.3 nm
Full Field of View	$20^{\circ} \times 6^{\circ}$ (350mrad x 100mrad)
Angular Resolution	$\sim 1\text{mrad}$
Bands (Spexels)	640
Positions	480
Lines (available)	$351 \geq ZZZ$
Mode of Operation/ DATA output	SNAP/ 640x480x1 data array SCAN/ image cube (640 x 480 x ZZZ)

Table 3.1. NUVIS parameters. From Cleary, 1998.



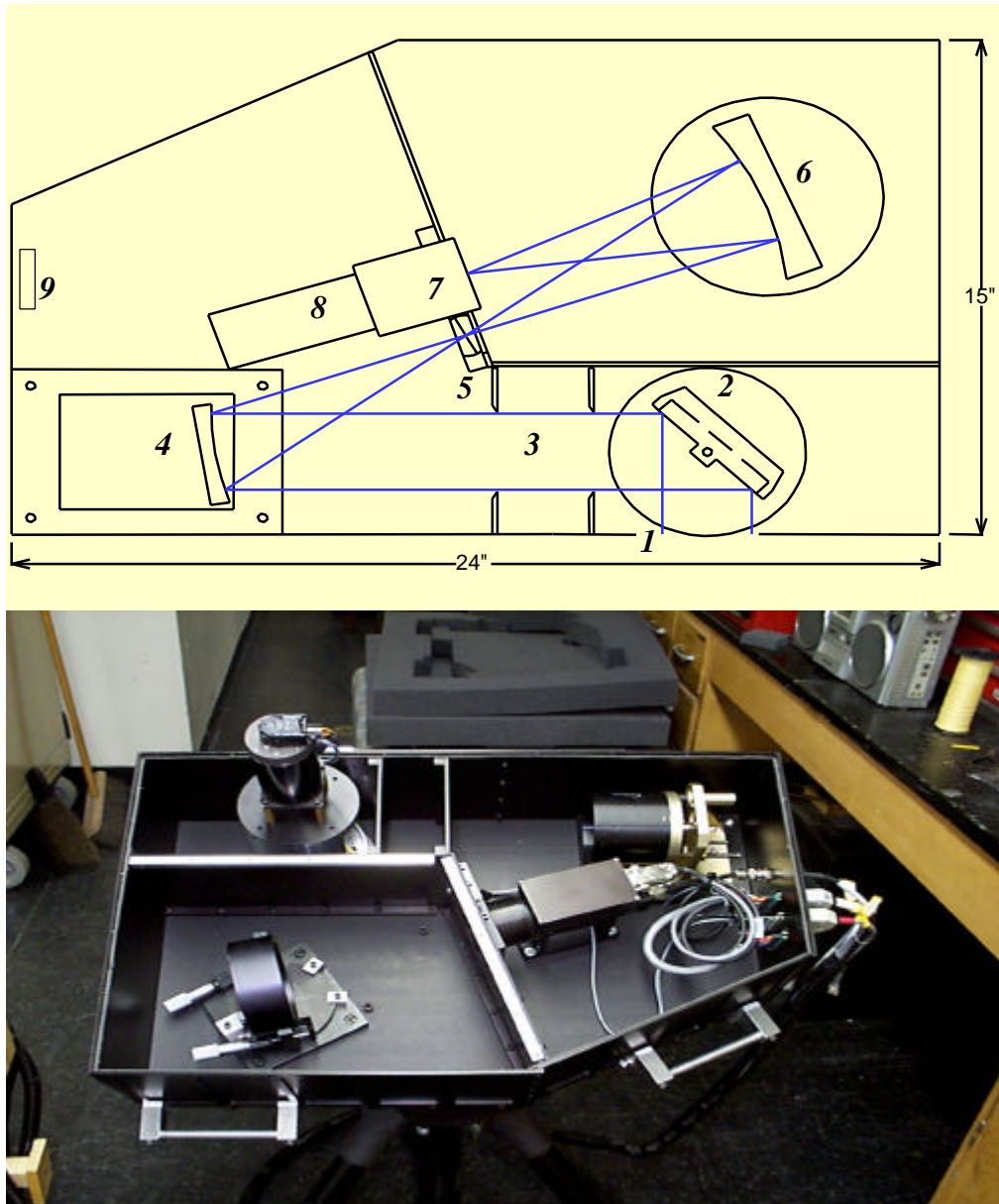


Figure 3.2. NUVIS components. Top: Schematic of NUVIS: 1) filter window, 2) scanning mirror assembly, 3) baffles, 4) telescope mirror, 5) slit, 6) diffraction grating, 7) image intensifier, 8) CCD camera, and 9) cable connectors. Bottom: Photo of NUVIS instrument components. (with cover removed)

rotates the mirror, and 3) the shaft encoder, which provides feedback information about the angular position of the mirror. Light reflected by the scanning mirror strikes a telescope mirror, which focuses the beam onto the entrance slit, which is located on the Rowland circle. From the slit, light travels to a field-flattened spherical diffraction grating. The diffracted light then goes to an image intensifier. The image intensifier, optimized for UV operation, optically amplifies the signal by a factor of nearly  $10^6$ . The image intensifier's output is coupled to a Pulnix TM-745e charge coupled device (CCD) video camera. The camera has 768 by 494 pixel resolution with  $11\mu\text{m}$  by  $13\mu\text{m}$  pixels. The camera output is conventional NTSC 30 frames per second (fps) analog video through a standard RS-170 interface and is limited to an eight bit grayscale and a resolution of 640 by 480 lines. (Hooks, 1997)

### **C. THE COMPUTER, DATA ACQUISITION AND CONTROL SYSTEMS**

The next major component of the total NUVIS system is the NUVIS data acquisition and control computer, including the CPU, monitor and supporting peripherals. The 233 MHz PENTIUM Pro PC includes 256Mb Ram and a 3.0 GB hard drive. It is equipped with standard 3.5 floppy and CD-ROM drives as well as a 1 GB internal JAZ drive. The video output from NUVIS's camera is processed into digital form by a PC IMAQ-1408 frame grabber interface card. Interfaces to the stepping motor controller and shaft position encoder are provided by DAC-02 and PIO-24ISA/EISA cards. The monitor is an NEC Multisync LCD 15 inch flat screen display. Figure 3.3 illustrates external views of the computer system.



CPU, Monitor, keyboard, and mouse. Note that all components are easily operated while still inside the customized shipping case.



Back panel of CPU with network hub attached. DAC-02 , PIO-24ISA/EISA & the PC IMAQ-1408 frame grabber cards displayed from the bottom up.

Figure 3.3. NUVIS control computer.

Control of the scanning mirror drive mirror drive is provided by the MAX-410 stepper motor controller that is illustrated in Figure 3.4. Figure 3.5 shows the complete NUVIS system deployed in the field, demonstrating some of the logistics and setups involved with on-site operations. A detailed account of suggested system components required for field operation can be found in the NUVIS field checklist of Appendix A.

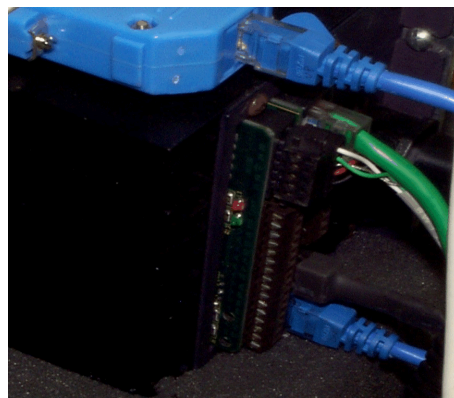
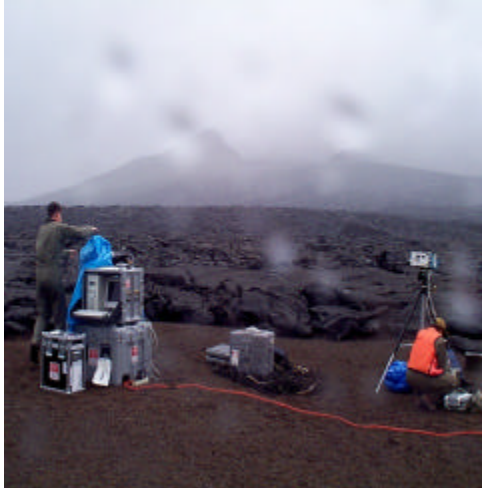


Figure 3.4. Max-410 stepper controller.



Left: Volcanic Site

Right: Power Plant Site

Figure 3.5. NUVIS system components and field logistics.

#### **D. DATA ACQUISITION, CONTROL AND DATA DISPLAY SOFTWARE**

As NUVIS was being developed, several key software routines were developed for instrument control, data acquisition and data display. Various modules of this software were written in Microsoft Visual Basic and Interactive Data Language (IDL), which is a Research Systems, Inc. (RSI) product. Specifics of the software may be found in the following references: Hooks, 1997; Aitken, 1997; and Using IDL, 1997 as well as in Appendix B.

In essence, the acquisition of spectral image data with NUVIS is a simple algorithmic loop. The scanning mirror is rotated so that one edge of the target scene of interest falls on the instrument's entrance slit. The diffraction grating then disperses the light from the slit across the camera. Because the Rowland circle spectrometer is stigmatic (image-preserving), the resultant 2D image consists of spectral information along the dispersion axis as a function of 1D scene height along the orthogonal axis. In other words, an image frame consists of a set of spectra for each scene pixel focused on the entrance slit. Each of these scene pixels, however, belongs to only a narrow vertical strip of the whole target scene. So, the camera frame is stored, then the scanning mirror is rotated slightly to position the next vertical strip of the scene onto the exit slit, and the frame acquisition procedure is repeated. This sequence of operation is repeated until data from the entire scene has been acquired. Subsequent off-line processing can then be used to generate a hyperspectral cube data set and to display the data in various formats.

Sample output from a field deployment is provided in Figures 3.6 through 3.8. This particular set is drawn from data taken of an industrial coal burning power plant. The image scene includes three operating smokestacks. All three stacks are producing some level of sulfur dioxide emissions, as well as a number of other effluent products. Two of the stacks have modern to contain SO<sub>2</sub> scrubbers that reduce emission levels. The third (dirty) stack emits SO<sub>2</sub> at levels on the order of ten times the ppm values of the scrubbed stacks. This particular collection was conducted on site at a range of 1.5 km. (Further detail of this field collection may be found in Chapter V.)

The black and white image of Figure 3.6 is produced directly from the sensor's recorded digital signals through a transpose, rotation and resizing of the data array. Although the stacks are quite visible, this format does not provide enough information to allow for the isolation and identification of SO<sub>2</sub> signatures in the data. A false-color



Figure 3.6. NUVIS black and white image. This image was produced by the IDL procedure, *Bw\_roughimage.pro*. From Cleary, 1998.

image can also be created to survey the data. This was done for the power plant work, using color assignments:

Red : 350-375nm,

Green: 325-350nm,

Blue : 300-325nm.

This approach results in the false color image of Figure 3.7, in which potential regions of sulfur dioxide appear yellow in color.



Figure 3.7. NUVIS false-color image. This is a product of the IDL procedure, "color\_image.pro". Regions of  $\text{SO}_2$  appear yellow in color. From Cleary, 1998.

Field operation of NUVIS necessitates a means of obtaining quick looks at the data in order to ascertain whether or not the instrument is functioning properly. An IDL procedure was developed to allow this. It performs a least-squares fitting of the data to a modeled absorption cross section of  $\text{SO}_2$ . Output displays from this procedure are illustrated in Figure 3.8. This corresponds to 200 different spatial (altitude) vs. spectral (wavelength) slices of the hyperspectral image cube. For presentation purposes, data

processing has been interrupted midway through the scene at line number 99 to illustrate the output windows presented to the data analyst. Window 1 shows a display similar to that of Figures 3.6 and 3.7. During the execution of this procedure, processing is actively displayed from right to left. A full false-color image of the scene is first presented and is then actively processed, scan by scan (line by line) within the window. The display labeled as Window 2 represents the raw data or digital number that is recorded for each individual pixel in the spatial (altitude) vs. spectral (wavelength) slice (plane), corresponding to line number 99. The raw data displayed on the right, corresponds to the line dividing the color and black and white images in the window on the left. This line marks the point at which the image cube was sliced to produce such a display. Within Window 2, the darker pixels represent lower levels of detection. The opposite is true for the brighter pixels.

Window 2 also parallels the actual raw data display that is presented to the user during instrument operation. This raw display is the only real-time feedback provided during system operation. Feedback is provided through the NUVIS operational window, which is displayed by the Visual Basic instrument control program *NUVIS.EXE*. A view of the same data at a time later in analysis process is presented in the lower windows one and two. Thus, Figure 3.8 also illustrates the representative output at the 150<sup>th</sup> vertical scan line.

In the field, the data acquisition and control PC can be networked to another computer, typically a laptop PC. The various IDL data analysis and display procedures



can then be run on the laptop while the host PC is otherwise occupied with running the instrument. This provides a quasi-real-time means of verifying NUVIS's operation in the field.

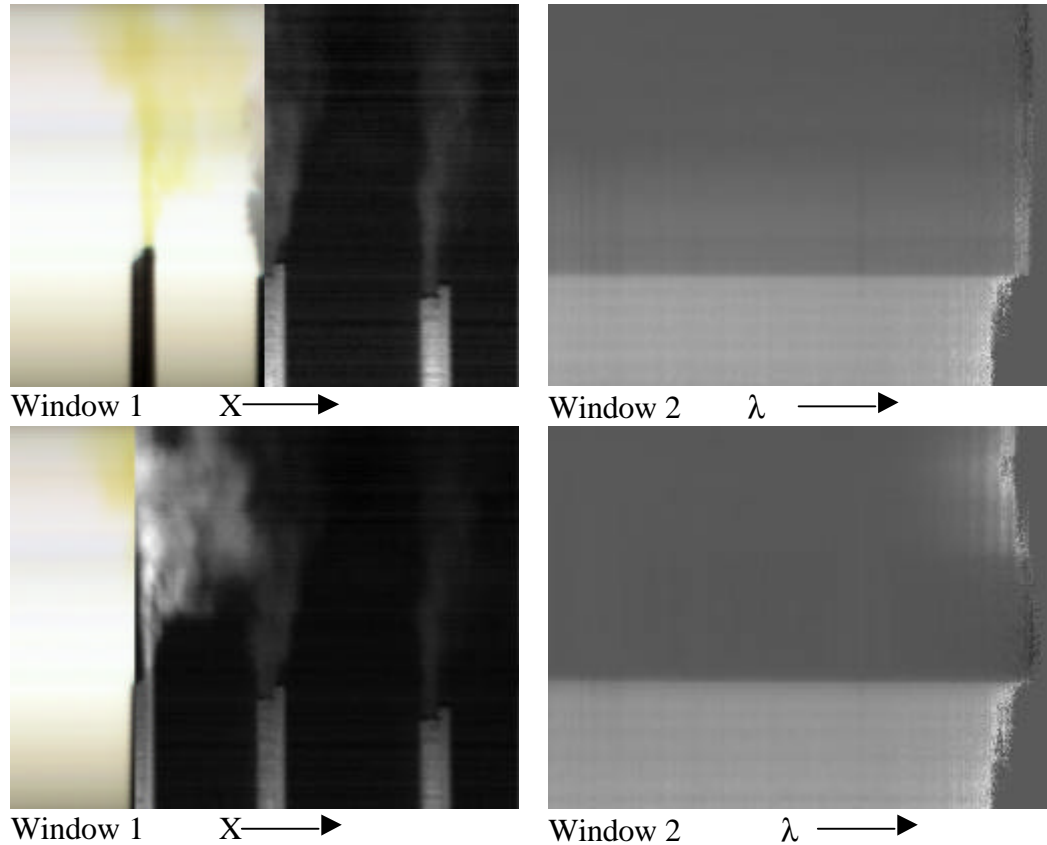


Figure 3.8. SO<sub>2</sub> algorithm output. Upper Windows demonstrate output displays for the 99<sup>th</sup> vertical line scan of the image scene during execution of the algorithm, "assay\_image.pro." Lower windows demonstrate processing some time later at the 150<sup>th</sup> scan position. In each case, altitude is displayed in the vertical (spatial-Y) direction. From Cleary, 1998.

THIS PAGE INTENTIONALLY LEFT BLANK

## **IV. LABORATORY CALIBRATIONS OF NUVIS**

### **A. PURPOSE**

In order for NUVIS to be applied to field measurements of SO<sub>2</sub> plumes, two types of calibrations must be performed, either beforehand or on site during field deployment. First, an approximate spectral wavelength scale must be established, so that spectral signatures of interest can be reliably and reproducibly identified. Second, the relevant curves of growth for the signatures must be available so that the instrument can be employed for reliable and credible spectrochemical abundance measurements. This chapter summarizes the laboratory calibrations that were performed in these contexts. The next chapter discusses applications of the calibrations to actual field data.

### **B. WAVELENGTH CALIBRATION**

Before continuing onto generation of the curves of growth, it is necessary to first discuss the association of instrument spectral samples (sometimes known as spexels) with wavelength. This phase of calibration was conducted by Dr. Cleary, just prior to my involvement with the NUVIS project. Results of the wavelength calibration were saved in a 1.2 MB data file entitled *wl\_cal.dat*.

The calibration was accomplished using a standard spectroscopic emission line source. The source used was a platinum (Pt) hollow cathode lamp, whose characteristics and calibration are traceable to the National Institute of Standards and Technology (NIST). This source was chosen because it exhibited a number of useful spectral emissions in the 300 to 400nm wavelength range. This particular lamp is used in

conjunction with a Harrison 6522 DC power supply. For operation, the supply is initially set at 400 volts and 0mA. The current is gradually increased to the operational level of 15mA. Nine Pt emission lines were identified and utilized in the calibration. These lines are listed in Table 4.1.

Line	Wavelength	Line	Wavelength	Line	Wavelength
1	304.26	4	337.82	7	359.36
2	306.47	5	340.81	8	369.42
3	334.54	6	352.05	9	372.71

Table 4.1. Nine platinum emission lines chosen for the wavelength calibration.  
From Cleary, 1998.

As with any diffraction grating instrument, the grating equation applies. (For further explanation see both MacMannis, 1997 and Hecht, 1998.) This means that the actual wavelength of a spectral feature should be a sinusoidal function of its position (spectral sample) in the measured data frame. It was found experimentally, however, that the sinusoid could be adequately approximated by a linear fit across the 300 to 400 nm range. This behavior is summarized in Equation 4.1

$$\mathbf{Y} = (0.118) \mathbf{x} + 300.775, \quad (4.1)$$

where  $\mathbf{x}$  is the spixel number,  $\mathbf{m}$  the spectral dispersion,  $\mathbf{b}$  the wavelength of the “zeroth” spixel and  $\mathbf{Y}$  is the corresponding wavelength in nanometers. This behavior is also illustrated in Figure 4.1. This calibration was applied in all instances where it became necessary to associate wavelength to a corresponding spectral sample. It also provided a

simple means for calibrating the wavelength scales of spectra measured with NUVIS, provided that the optomechanical configuration of the instrument remained stable.

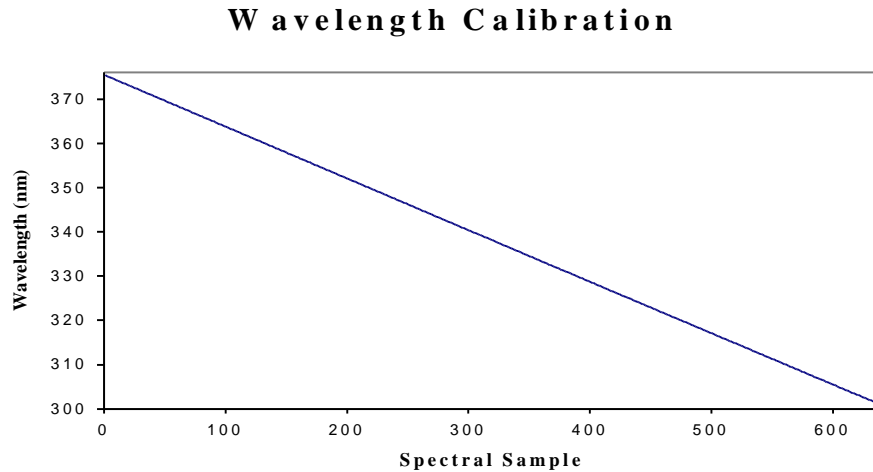


Figure 4.1. Wavelength calibration associating band number/spixel to wavelength.

### C. EXPERIMENTAL OVERVIEW

As stated earlier, only absorption lines existing longwards of 305nm were chosen for laboratory measurement because absorption lines that appeared in the field data at shorter wavelengths were either saturated or subject to severe noise because of rapidly decreasing background illumination. Figure 4.2, vividly demonstrates the relatively closely spaced group of absorption lines that were targeted for calibration. In the end, four absorption lines were identified as suitable for equivalent width measurements in the calibration. The spectral sample numbers and wavelengths corresponding to the centers of each of these absorption lines are listed in Table 4.2. Because NUVIS was expected to

operate over a wide range of column densities, the decision was made to first concentrate on the instrument's lower sensitivity limits.

### Measured SO<sub>2</sub> Absorption Lines

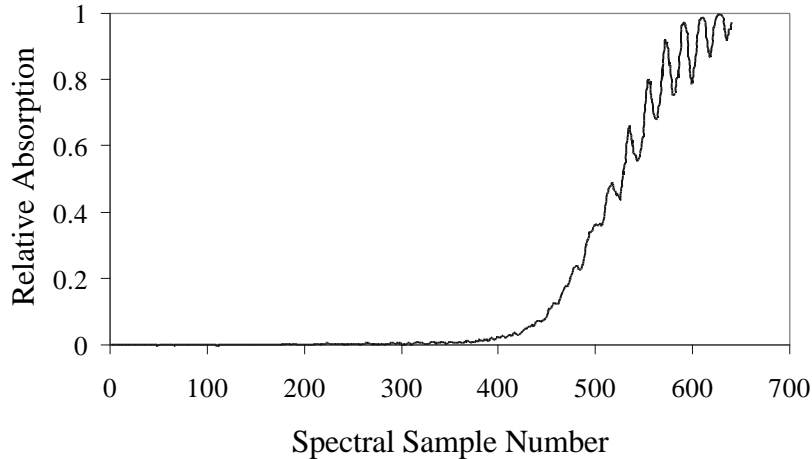


Figure 4.2. Example of SO<sub>2</sub>'s closely spaced absorption lines. In this plot, lower spectral sample numbers equate to higher UV wavelengths and higher numbers equate to lower ones. See Figure 4.1.

Measured Absorption Line #	1	2	3	4
Spectral Sample Number	535	554	572	590
Center Wavelength (nm)	313	310.9	308.8	306.5

Table 4.2. Absorption lines targeted for measurement.

#### D. LABORATORY MEASUREMENTS OF SO<sub>2</sub>

There are two constraints on the gas concentrations that are useful for laboratory calibration studies. First, the experimental noise floor sets a practical lower limit to the instrument's sensitivity. That is, weak spectral features that are buried in the noise must

simply go unmeasured. This translates into a lower useful limit to SO<sub>2</sub> concentrations used in the laboratory. Second, as discussed earlier, highly saturated spectral features do not provide reliable measurements of spectrochemical abundance, and so should be avoided. This sets a practical upper limit on laboratory gas concentrations. After weighing such considerations, six SO<sub>2</sub> column abundances were decided upon for study. They are summarized in Table 4.3.

Sample	Column abundance (∞ concentration) [(#molecules/m <sup>3</sup> m)]
1A	$5.33 \times 10^{21}$
2B	$5.61 \times 10^{21}$
3A	$7.48 \times 10^{21}$
3A	$1.07 \times 10^{22}$
4B	$2.25 \times 10^{22}$
4B	$4.24 \times 10^{22}$

Table 4.3. The six test cell concentrations utilized in generating the curves of growth.

### 1. Gas Test Cells

SO<sub>2</sub> was placed in transparent test cells of various lengths and illuminated with UV continuum radiation to produce laboratory spectra. The first test cell employed was a 1.55 meter long PVC tube with quartz windows (see Figure 4.3). Once evacuated with a conventional fore pump, the cylinder could be filled through a pressure regulator with 0.11 % sulfur dioxide in an inert dilution gas (N<sub>2</sub>). The valve manifold and Matheson pressure gage ( 0 to 760 mm Hg ) that were both utilized in this process are illustrated in Figure 4.4. For various reasons, the 1.55 m cell proved to be cumbersome, prone to

leaks, and too long for producing low column abundances of  $\text{SO}_2$ . Therefore, another test cell was designed.

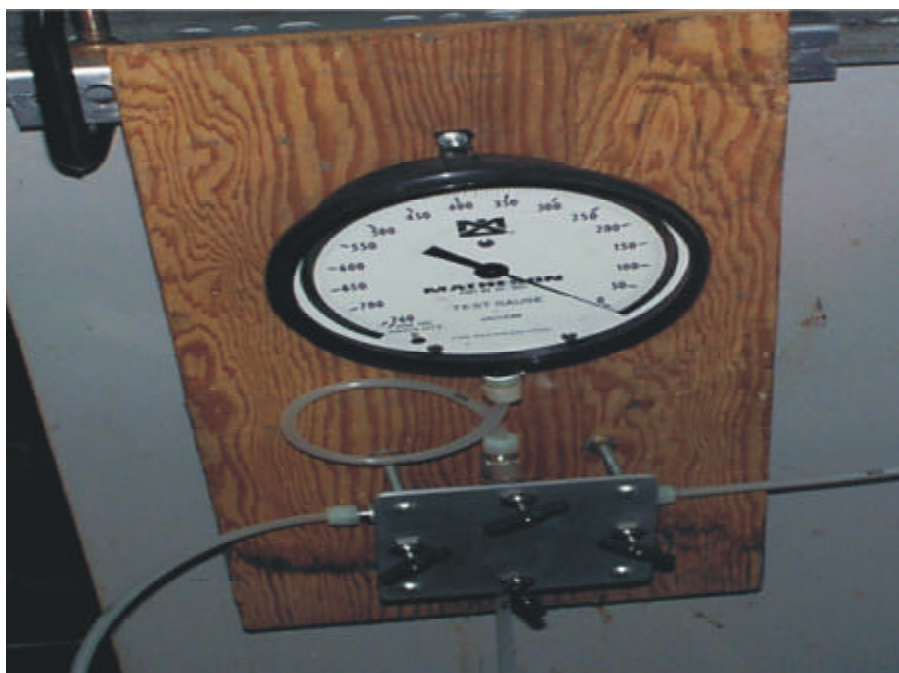


Figure 4.3. Pressure gage and valve manifold.

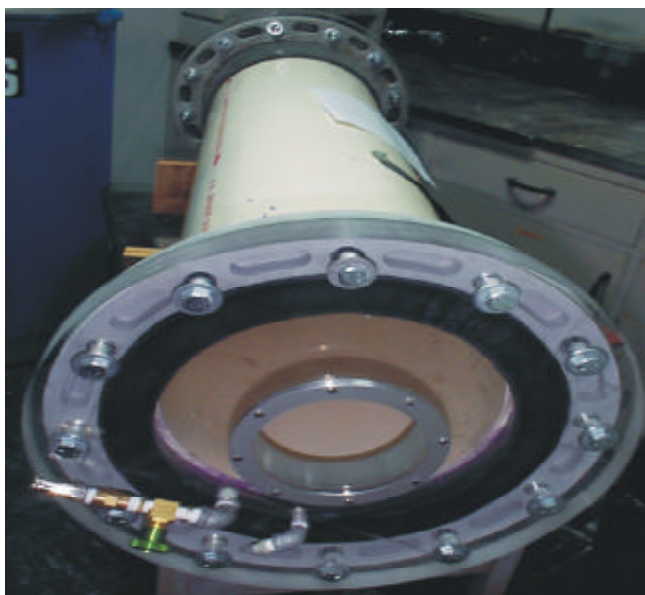


Figure 4.4. 1.55 m gas test cell #1.



The next test cell was considerably shorter and more portable, and could potentially be utilized not only in the laboratory but also in the field. It is illustrated in Figure 4.5. Even though this design was more portable than the first, it was quickly abandoned for two reasons: 1) The test cell could not reliably be coupled to the optical entrance (filter window) of NUVIS. 2) The cell combination was mechanically unstable and could potentially damage the instrument's filter window.

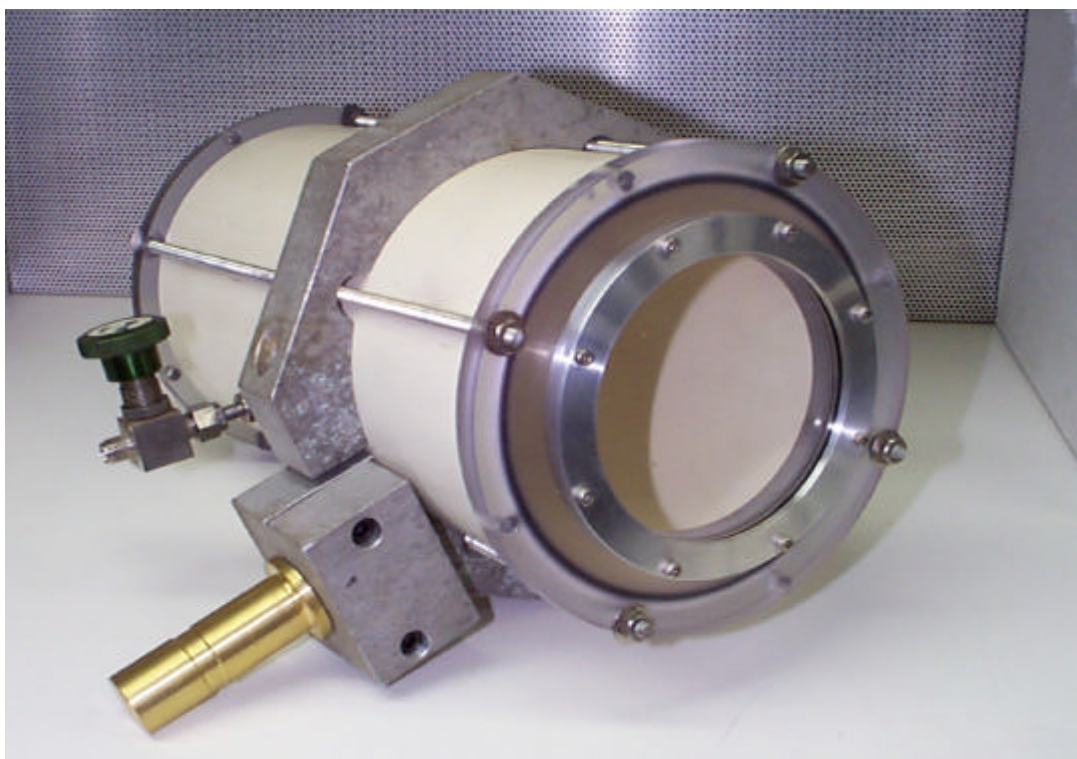


Figure 4.5. Gas test cell #2.

To remedy these differences with the first two gas test cells, it was decided to obtain a more enriched mixture of sulfur dioxide (Matheson 10% mixture in air) and to use much shorter gas test cells. Four inch diameter (10.16cm) by 3.25cm inner path length quartz cells were purchased from Weiss Scientific Glass Blowing Company. They are shown in Figure 4.6. These smaller cells also had a mechanical advantage: they can

be mounted easily at NUVIS's optical entrance filter window, permitting easy laboratory and field use. A minor difficulty with their use was discovered, however. Their available window diameter is only 8.77cm once the cell is installed in the shop fabricated aluminum housing/mounting. This cause slight vignetting at the corners of the instrument's field of view. During thesis research, care was taken to exclude these regions and a new set of six inch diameter test cells and associated mountings are under development. In Figure 4.7 a layout of the filter window and the gas test cells is shown.

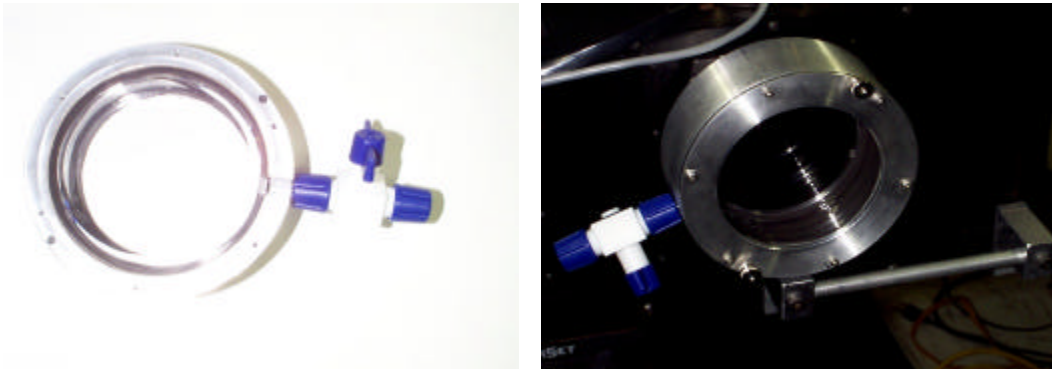


Figure 4.6. Four inch gas test cells. Photos taken before and after installation.

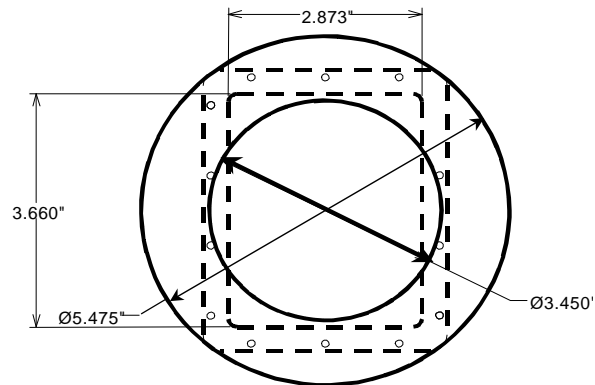


Figure 4.7. Test cell comparison. Dotted line represents NUVIS filter window. Circles represent available cross sections associated with the 4 inch (inner circle) and 6 inch (outer circle) cells respectively. The reduced cross sections are due to the cell mounts themselves.

The filter window is represented by a dotted line and the two circles (of diameter 3.45 and 5.475 inches, respectively) represent the available cross sections provided by the four inch and new six inch cells.

## 2. Calibration Source and Reflective Screen

During initial calibration attempts, an EG&G Gamma Scientific deuterium lamp was utilized as a background continuum illumination source. In the 300 to 375 nm spectral region, this lamp's maximum specific output irradiance was on the order of  $10^{-2}$  ( $\mu\text{W}/\text{cm}^2 \text{ nm}$ ). These source levels proved to be too low for practical absorption measurements in the laboratory. A 1000 Watt quartz halogen tungsten filament lamp (FEL-309 IR) from Optronics Laboratories was chosen to replace the deuterium lamp. It is a NIST traceable UV source and was utilized throughout all calibrations. The spectrum of this source is illustrated in Figure 4.8.

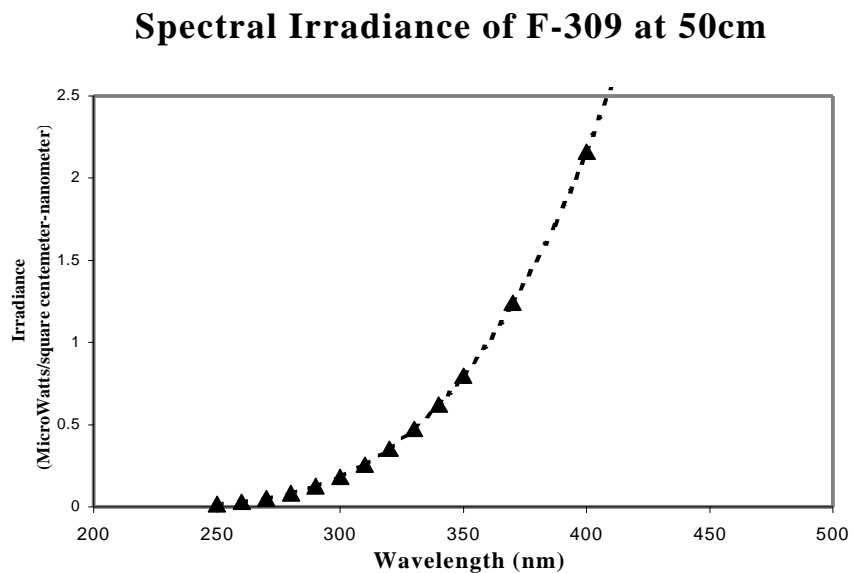


Figure 4.8. Spectral irradiance of FEL calibration source over operational NUVIS wavelengths.

The lamp was mounted in an enclosed box with a controllable output aperture, which was used to maximize the optical fluence on a diffuse reflective screen, described below. The lamp was powered by a Hewlett-Packard 6030-A power supply. Maximum drive current was set to 8.0 amps. The lamp required a 15 minute warm up period (according to the manufacturer) to achieve steady state operation before measurements could be taken.

The light from the FEL lamp was scattered by a reflective screen assumed to be an ideal diffuse Lambertian surface (see Hecht, 1998). The screen was a Spectralon diffuser with greater than 97% reflectivity in the wavelength region of interest ( see Figure 4.9 ). It was placed 150 cm from the FEL and approximately normal to the

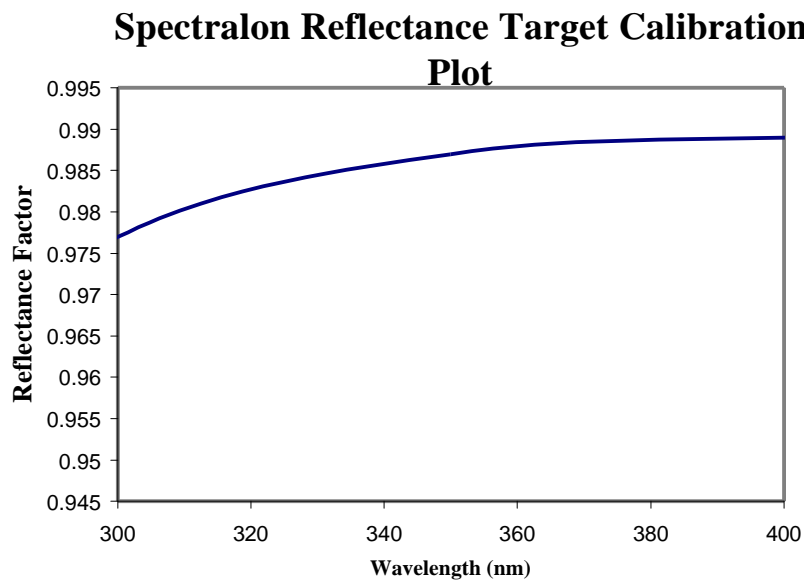


Figure 4.9. Screen reflectance values.

lamp-screen axis. The NUVIS instrument was oriented at 45 degrees from this normal axis. The geometry of the setup is illustrated in Figure 4.10.

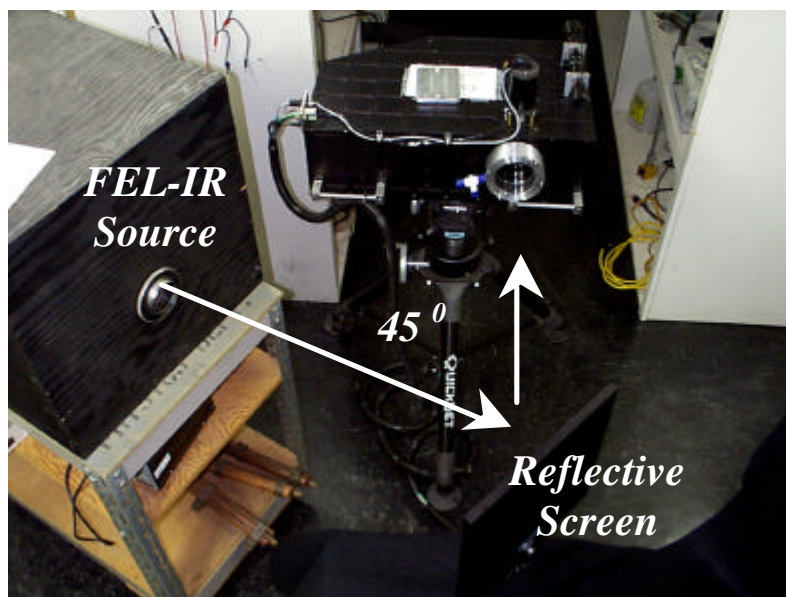


Figure 4.10. Experimental set up. Instrument is placed at 45 degree angle from screen-lamp axis. UV source is enclosed by the box and is positioned for normal incidence to the screen.

### 3. Test Cell Preparation

Calibration cells were prepared by first connecting them to the valve manifold. A vacuum was drawn on the cell using a mechanical fore pump vented through a gas exhaust hood. The cell gas pressure was monitored by the Matheson pressure gage. For background calibrations, evacuated cells could be used. If the cell was to be filled with

sulfur dioxide, the appropriate concentration was introduced by using a standard gas regulator while monitoring the pressure.

The entire setup (see Figure 4.11) had some inherent limitations. The gage only marked pressures in increments of 5mm of mercury (mm Hg). This did not permit very precise determination of cell gas pressure and caused uncertainties in gas concentration, particularly at low pressure.

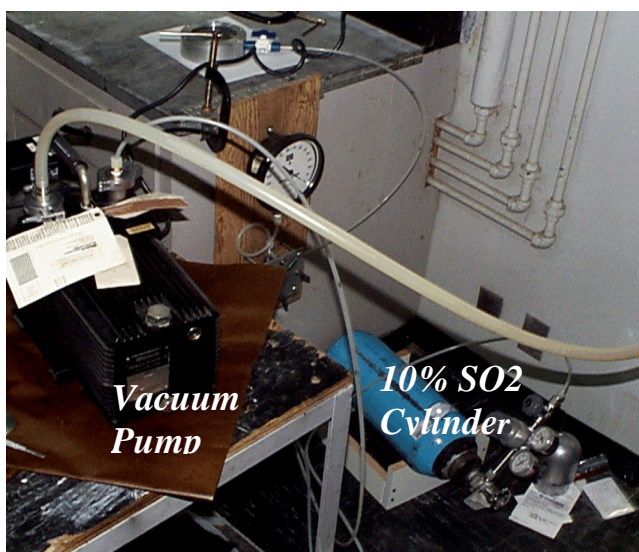


Figure 4.11. Cell preparation setup.

#### **4. Data Acquisition**

Once a cell was prepared, it was mounted in front of the filter window of the instrument. Because fluorescent lights exhibit well known emissions in the ultraviolet, the lab was darkened before measurements were taken. A range of instrument gains was first tested to determine where sensor saturation occurred. This was accomplished by using the VIDEO feature displayed in the NUVIS control window. An image intensifier

gain of 7.0 was set in the control window. Measurements were obtained by first setting the number of images per SNAP to 100. Spectra were then recorded using the NUVIS SNAP mode, in which the scan mirror is not rotated. In addition to gas spectra at each concentration, spectra of empty cells were recorded for comparison purposes. The spectra were saved to a 1 GB Jaz cartridge as a 30MB NUVIS file.

## **5. First Results**

For the first experiment, fifteen different spectra were recorded. Three representative spectra from experiment #1 are illustrated in Figure 4.12. These plots represent mean spectra calculated by averaging over all 480 pixels in the vertical image column and then averaging over all 100 images to enhance the experimental ratio. Only spectral samples  $\geq 500$  are displayed. As discussed earlier, absorption is characterized by the ratio  $I / I_0$ . Hence each SO<sub>2</sub> spectrum was then divided by the corresponding spectrum of the evacuated cell. The results are illustrated in Figure 4.13. Neither of these initial spectrum exhibited identifiable SO<sub>2</sub> spectral absorption features. This demonstrated that the sensitivity of NUVIS was insufficient to detect SO<sub>2</sub> at column abundances on the order of approximately  $10^{20}\text{m}^{-2}$ .

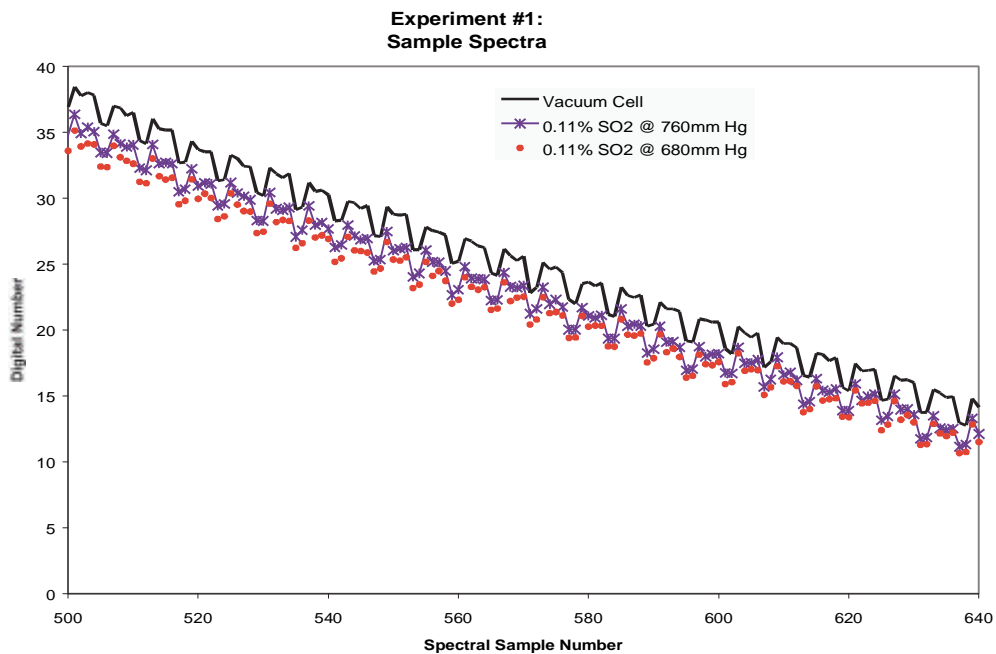


Figure 4.12. Sample spectra of experiment #1 including measurements from one evacuated cell and two SO<sub>2</sub> test cells.

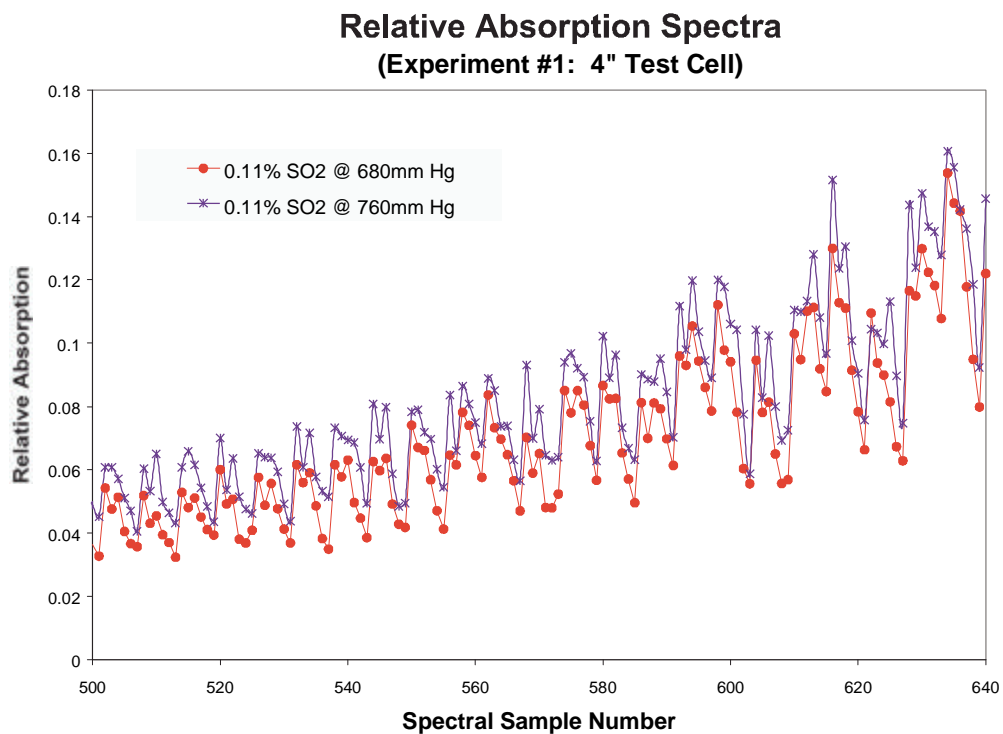


Figure 4.13. Relative absorption spectra of experiment #1.



## E. GENERATING EXPERIMENTAL CURVES OF GROWTH

### 1. Approach

A second set of experiments was undertaken with higher concentrations of SO<sub>2</sub>. Various concentrations were tried until unambiguous detection of SO<sub>2</sub> spectral features was assured. Given the limitations of the pressure gage, described above, and the availability of only 0.11% and 10% SO<sub>2</sub> mixtures, the range of reliable gas abundances in the cells was somewhat restricted. But, when data from these abundances were combined with those from earlier measurements using the 1.55 m cell, enough data points for the generation of calibration curves of growth were achieved. The details are summarized in Table 4.4. The second experiment was initially designed to increase test cell concentration in an attempt to see the first signs of absorption line formation. Increasing cell concentration meant utilizing the 10% SO<sub>2</sub> as the test source. Unfortunately, the restrictions imposed by the Matheson gage setup (Figure 4.4) limited the four inch test cell to be backfilled with 10% SO<sub>2</sub> only as low as 50 mm Hg. This was the lowest achievable concentration with the existing pressure regulator, gage and valve manifold. Details of all cell parameters and concentrations utilized in generating the curves of growth may be found in Table 4.4.

Sample Number	Cell	Source (%SO <sub>2</sub> )	Pressure (mm Hg)	Path length (m)
1A	4"	10	50	.0325
2B	1.55m	0.11	100	1.55
3A	4"	10	70	.0325
4A	4"	10	100	.0325
5B	1.55m	0.11	400	1.55
6B	1.55m	0.11	760	1.55

Table 4.4. Cell parameters utilized in generating the curves of growth.

## 2. Experimental Results

The resultant raw spectra of experiment #2 are illustrated in Figure 4.14. When these SO<sub>2</sub> spectra are ratioed with their corresponding evacuated cell spectra, the ratio spectra of Figure 4.15 are generated. These spectra are plotted along with three additional absorption spectra (calculated from the Cleary data sets) in Figure 4.16. The data sets are marked A (new) and B (old) data respectively. They have been adjusted

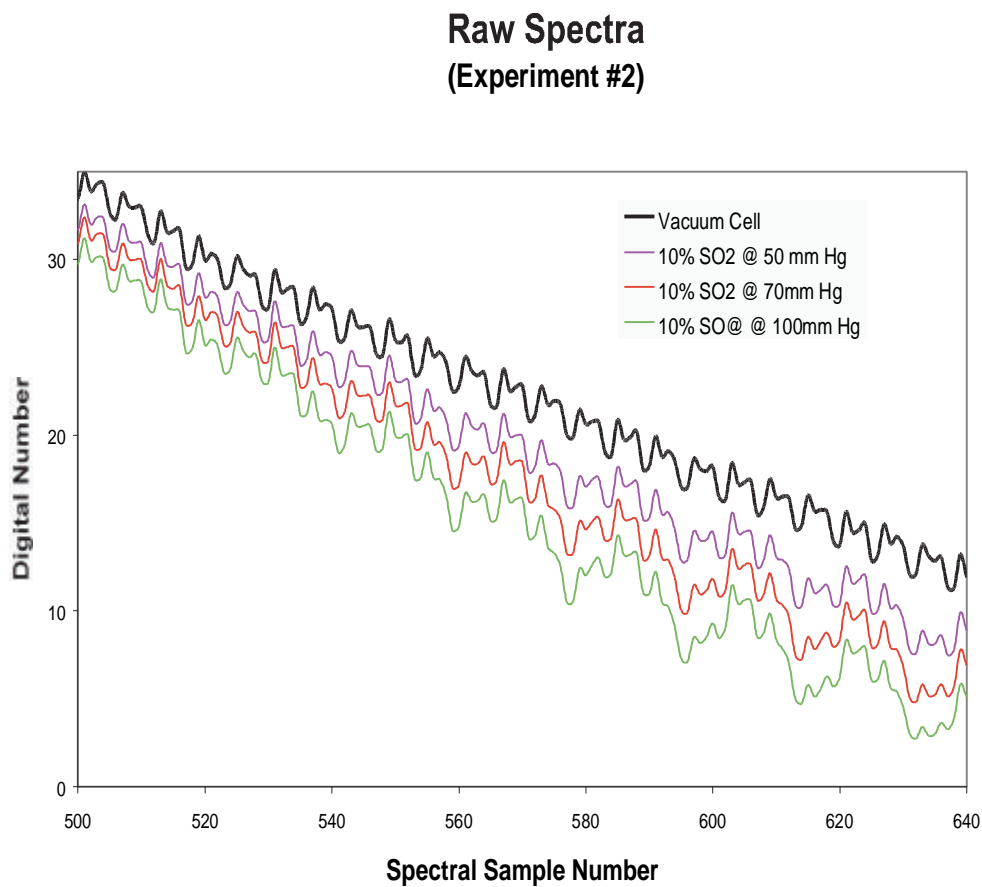


Figure 4.14. Raw spectra from experiment #2, including measurements from one evacuated and three SO<sub>2</sub> test cells.

### Relative Absorption Spectrum (Ratio Spectra from Experiment #2)

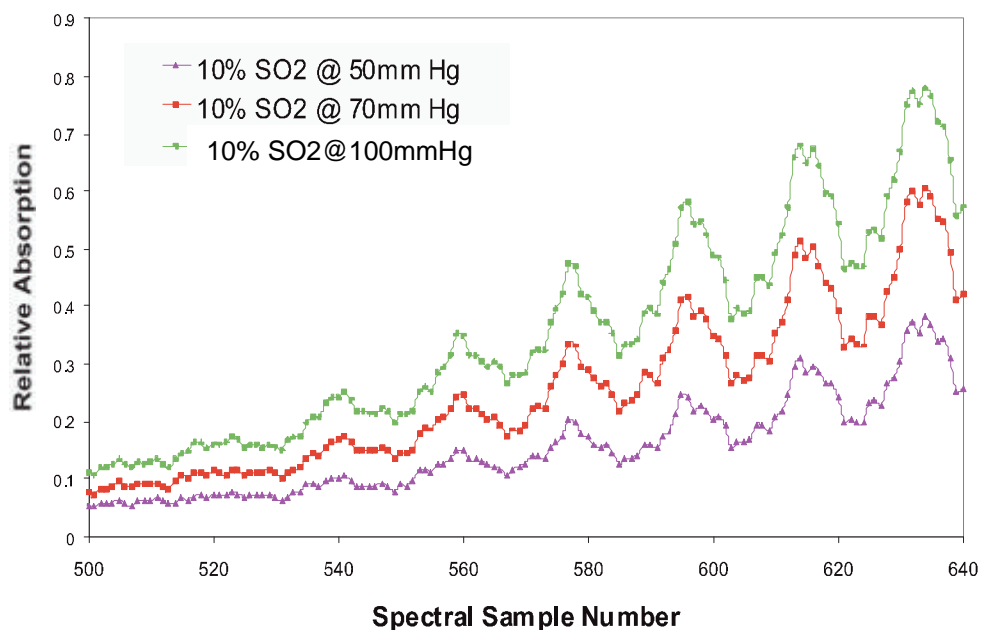


Figure 4.15. Relative absorption spectra from experiment #2.

### Relative Absorption Spectra (Ratio Spectra from Combined Data Sets)

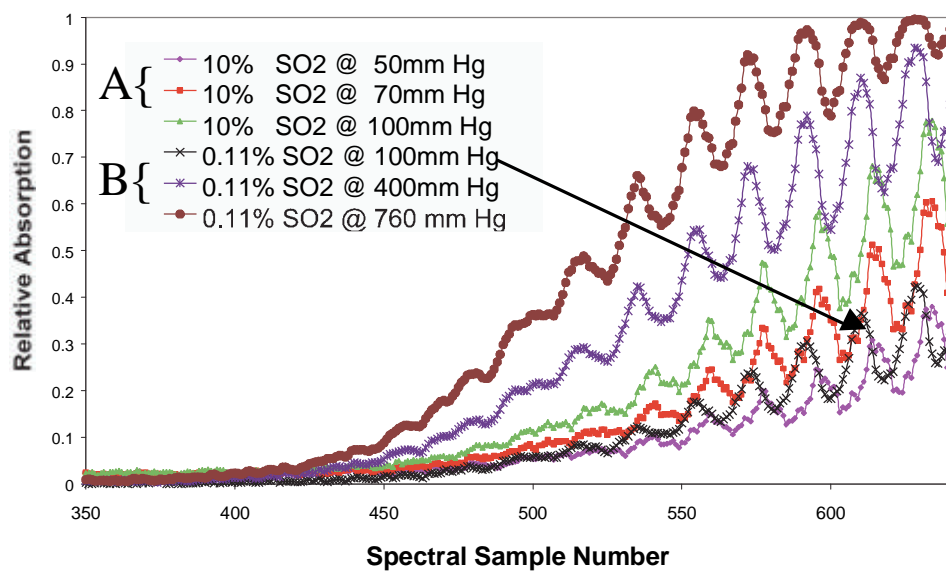


Figure 4.16. Relative absorption spectra generated from combined data sets.

to the same baseline to compensate for instrumental gain drift effects and lamp fluctuations. It was also discovered that the new data set's spectral features were shifted by five spectral sample numbers from the earlier data. This was not too surprising, since the instrument had now completed four major field deployments and had experienced great deal of handling during shipment. To compensate, bands in the new spectra (Alpha data sets) were uniformly adjusted by five spexels to match the corresponding absorption lines of the old spectra (Beta data sets). Figure 4.16 displays three of the new data sets prior to adjustment (one is annotated with an arrow) to demonstrate this effect. The adjusted spectra are illustrated in Figure 4.17.

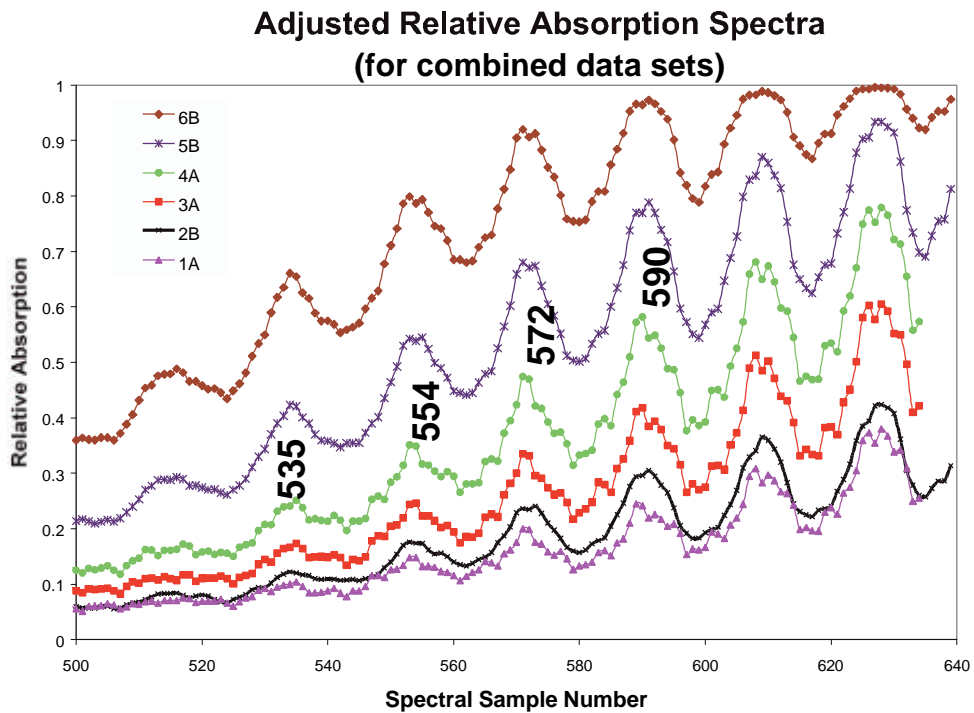


Figure 4.17. Adjusted relative absorption spectra. New data sets adjusted to account for wavelength shifts in the instrument. Please refer back to Table 4.4 for details on cell concentrations 1A through 6B.

### 3. Analysis of Experimental Data

The IDL procedure GAUSSFIT was utilized to fit individual Gaussian profiles to each of four absorption lines (centered about spectral sample numbers 535, 554, 572 and 590) in each of the six data sets. The resultant fits are illustrated in Figures 4.18 through 4.23. Their equivalent widths were calculated by integrating each Gaussian (24 in all) in accordance with Equation 2.9. Table 4.5 provides details for each of these 24 absorption lines. For each absorption line, six different equivalent width measurements were recorded, one for each SO<sub>2</sub> concentration. Equivalent widths were then plotted against cell concentration and resulted in the generation of four curves of growth. A least squares nonlinear fit has been performed to each of the four sets of measurements (at spectral sample numbers 535, 554, 472, and 590, respectively) using Mathematica to produce four modeled calibration curves. A summary of the resultant equations for each of the four models is provided in Table 4.6 and curves of growth are plotted in log-log scale format in Figures 4.24.

SO <sub>2</sub> Column Abundance (#molecules/m <sup>2</sup> ) x10 <sup>21</sup>		5.33	5.61	7.48	10.7	22.5	42.4
Nominal $\lambda$ :	Equivalent Width of Spectral Feature in nm at:	0.382	0.561	0.761	1.12	1.64	2.57
306.5 nm	Sample #590						
308.8 nm	Sample #572	0.375	0.396	0.576	0.673	1.06	1.40
310.9 nm	Sample #554	0.250	0.303	0.422	0.739	0.902	1.68
313 nm	Sample #535	0.211	0.281	0.384	0.505	1.05	1.39

Table 4.5. Line equivalent widths for measured absorption lines as a function of SO<sub>2</sub> column abundances.

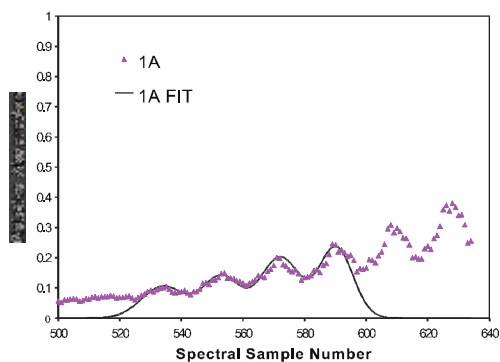


Figure 4.18. Concentration 1A

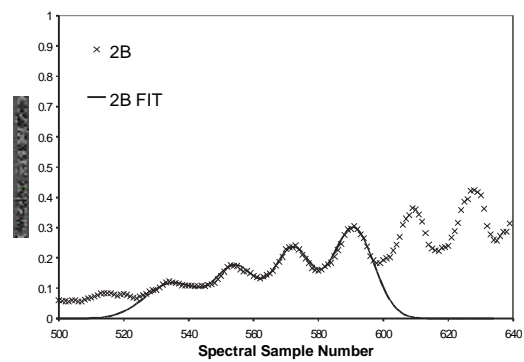


Figure 4.19. Concentration 2B

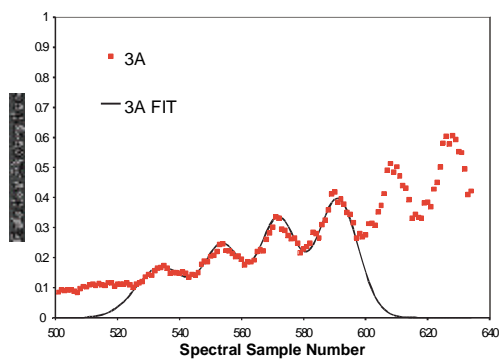


Figure 4.20. Concentration 3A

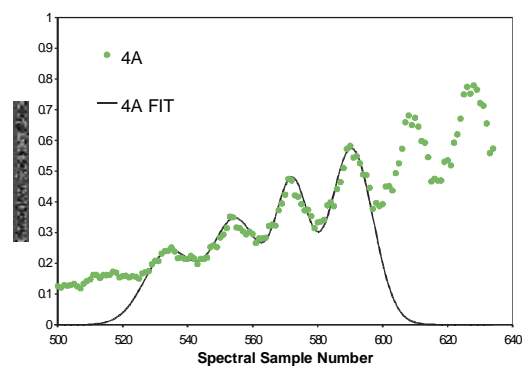


Figure 4.21. Concentration 4A

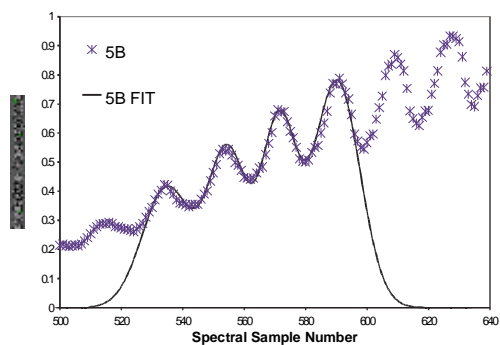


Figure 4.22. Concentration 5B

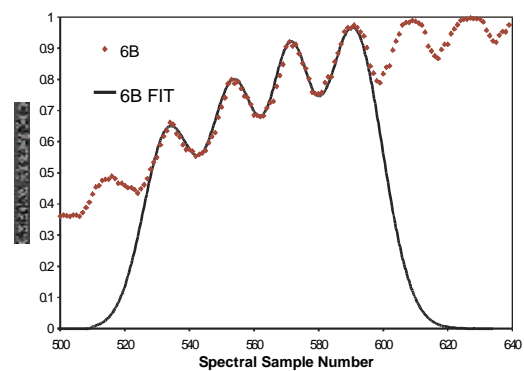


Figure 4.23. Concentration 6B

Sample Number of Spectral Feature	Equation for Modeled Curves of Growth
535	$W = -28.234 + 0.5685 \ln ( V )$
554	$W = -31.122 + 0.6268 \ln ( V )$
572	$W = -23.975 + 0.4867 \ln ( V )$
590	$W = -48.372 + 0.9754 \ln ( V )$

Table 4.6. Equations for modeled curves of growth.  
( $W$  is the equivalent width in nm and  $V$  is the column abundance in  $\text{m}^{-2}$ )

### Curves of Growth for $\text{SO}_2$

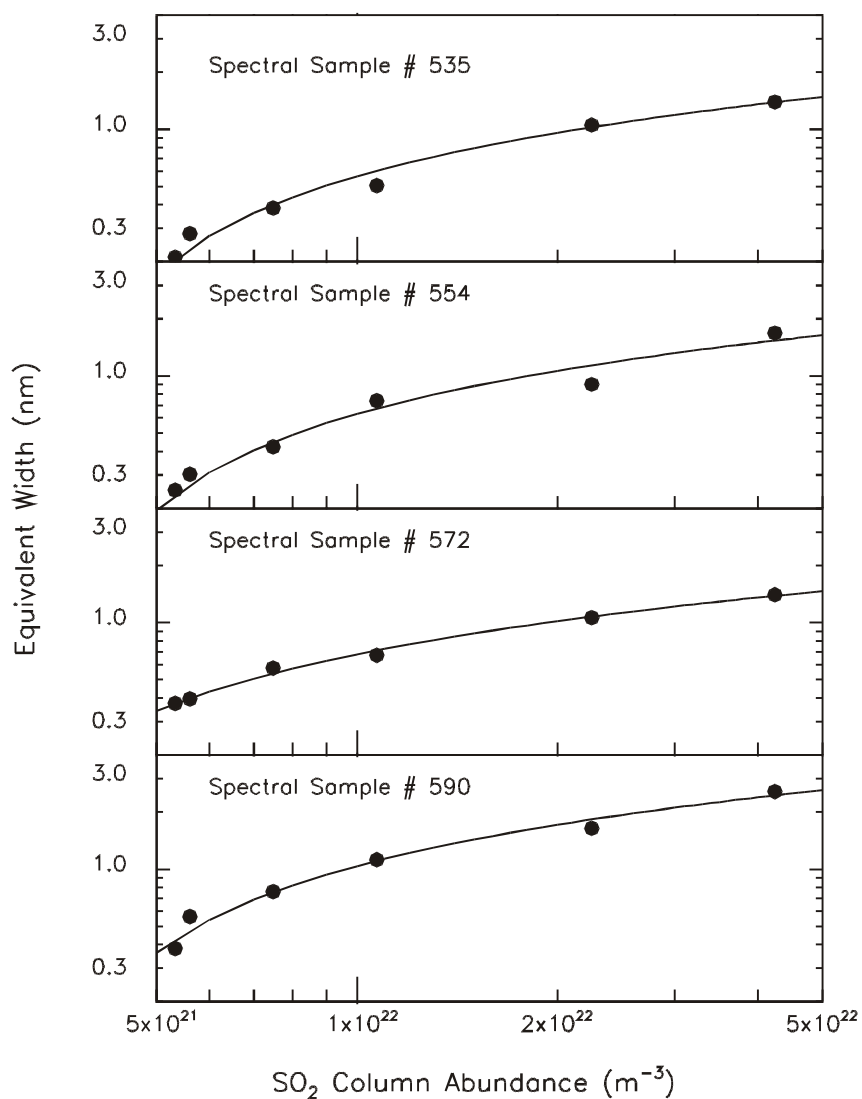


Figure 4.24. Laboratory generated curves of growth for  $\text{SO}_2$

THIS PAGE INTENTIONALLY LEFT BLANK



## **V. APPLICATION OF LABORATORY CALIBRATIONS TO FIELD DATA**

As stated earlier, the motivation for this thesis research has been the need to characterize and to quantify NUVIS's capabilities as a remote sensing spectrochemical analysis instrument. The completion of the laboratory calibration procedures described in Chapter IV now permit us to apply these quantitative calibrations to real field data.

### **A. FIELD EXPERIMENTS**

Data described in this chapter resulted from three separate field experiments with NUVIS. Two field collections were conducted in 1998, just prior to the inception of this thesis project. The third field collection was conducted in April of 1999 in direct support of this thesis research. Each of these experiments was conducted on site at a coal-firing power plant. The plant provided three operational smokestacks that were available for remote measurement through clear desert air.

During the 1998 collections, only two of the three operational stacks had operational SO<sub>2</sub> scrubbers. Thus, the third stack provided a much higher SO<sub>2</sub> plume signature than the other stacks. Direct *in situ* measurements provided by plant managers indicated that the clean stacks emitted SO<sub>2</sub> at levels in the tens of ppm (approximately 40 ppm). Similar measurements indicated that the unscrubbed stack operated with SO<sub>2</sub> emissions in the hundreds of ppm (approximately 100 to 400 ppm). Photos of the power plant may be found in Figure 5.1. There are actually six stacks in the image scene. Three of the six were recently built because of mandated reductions in pollutant emissions. (Cleary, 1998)



Figure 5.1. Coal burning power plant. Photos were taken during 1998 (left) and 1999 (right) collections. Only two of the three scrubbers were in operation in 1998 but in 1999 scrubbers were on-line in all three stacks.  
1998 photo courtesy of Cleary, 1998.

During the most recent on site field measurements, in the spring of 1999, the power plant had just brought the final set of scrubbers on-line. This meant that all three stacks emitted  $\text{SO}_2$  at or below 40 ppm concentration.

The acquisition of experimental field data followed a procedure much like that used in the laboratory, but with the following modifications: 1) NUVIS was operated in its full hyperspectral imaging mode, providing spectral information for each 2D image pixel. 2) The source of background continuum radiation, against which  $\text{SO}_2$  absorption was measured, was natural sky scattered UV solar radiation. Hence, each spectrum had to be ratioed with a clear sky spectrum in order to quantify  $\text{SO}_2$  absorption. Figure 5.2 shows a representative sky spectrum recorder in the field.

Figure 5.3 shows a corresponding spectrum for a region of an image including the effluent plume from a smokestack. It is evident that absorption features exist that are not

present in the clear sky spectrum. This is particularly obvious in Figure 5.4, where both spectra are plotted jointly. Figure 5.5 shows the ratio of the plume and clear sky spectra. The typical SO<sub>2</sub> spectral signatures are evident at the high spectral sample side of the plot. By fitting profiles to these signatures, calculating each profile's equivalent width, and comparing those with the calibration curves of growth, effective column abundances of SO<sub>2</sub> can, in principle, be determined.

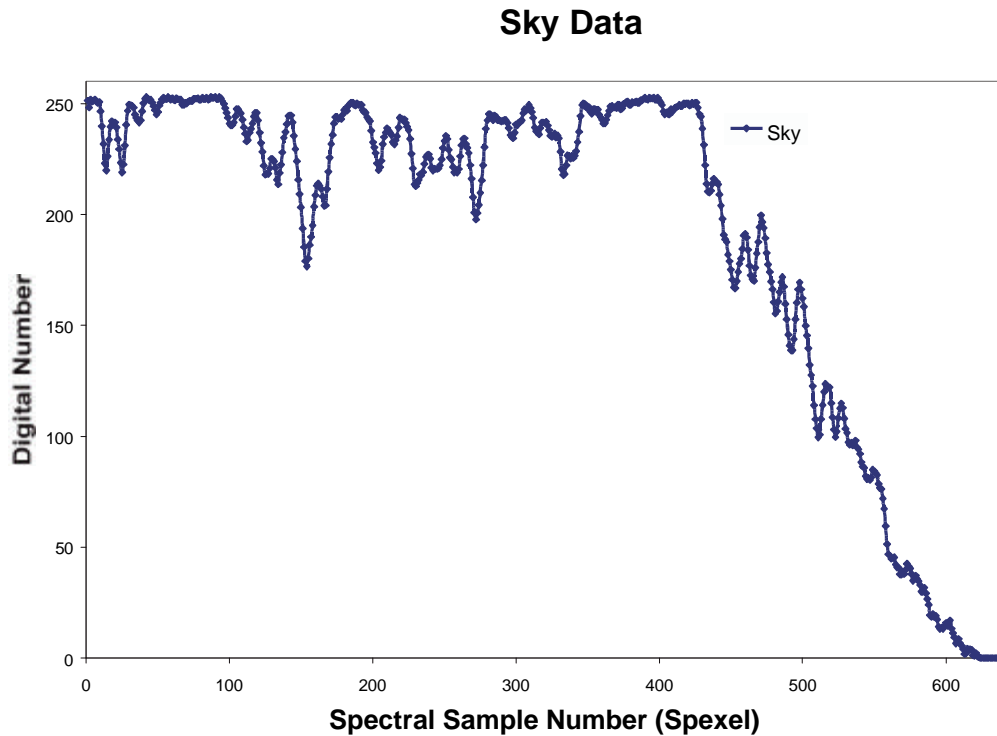


Figure 5.2. Sky spectrum recorded by NUVIS.

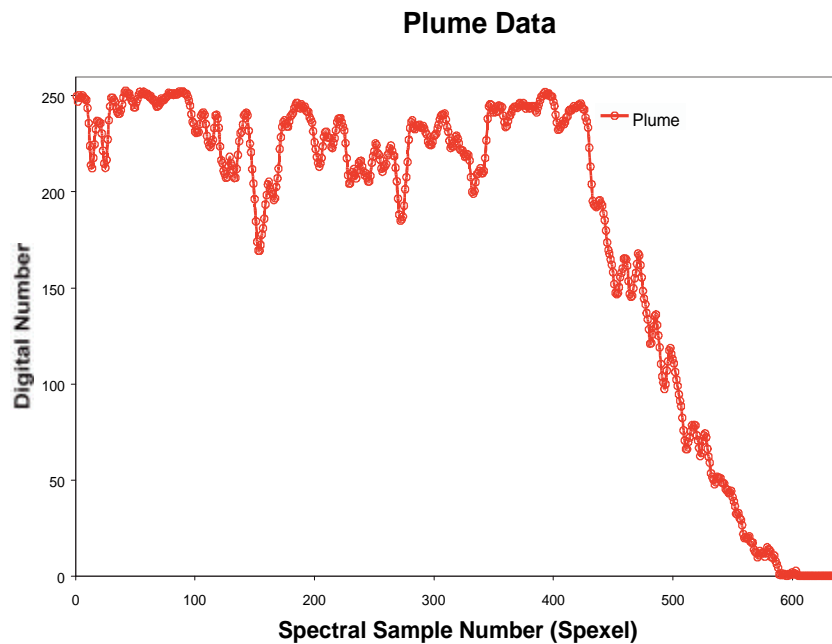


Figure 5.3. Spectrum from smokestack plume.

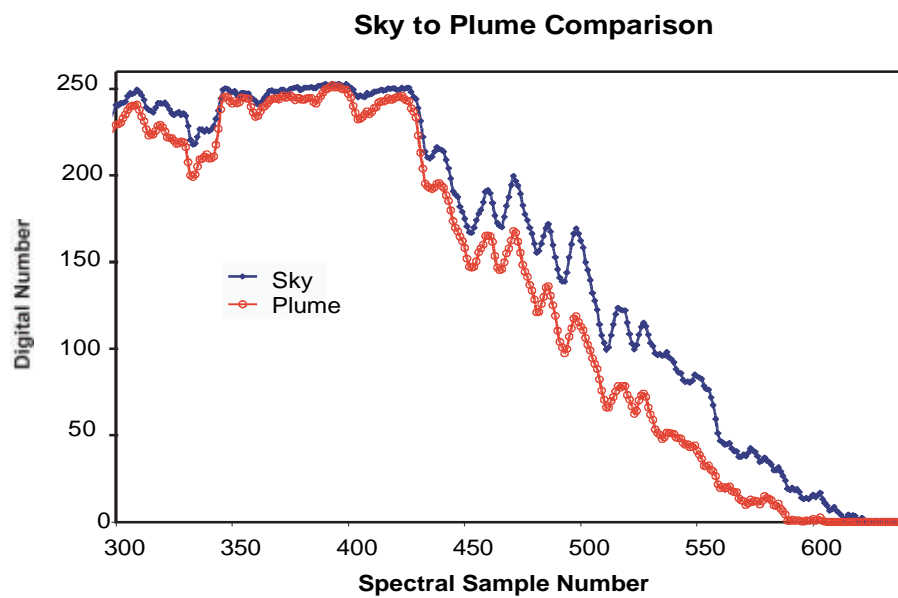


Figure 5.4. Sky and plume spectra comparison.

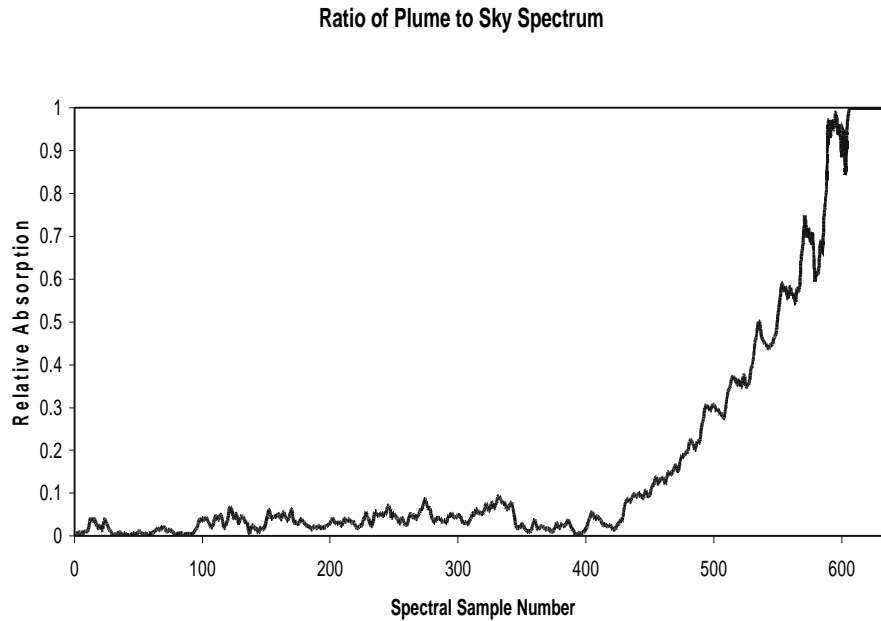


Figure 5.5. Plume-to-sky ratio spectrum. Values range from 0-1.0 corresponding to 0-100% absorption.

## **B. RESULTS**

In order to test the calibration procedure, representative sky and plume regions of interest (ROIs) were selected for the “dirty” stack from one of the 1998 data sets. This particular set was obtained at a range of approximately 0.2 km from the stack. Figure 5.6 illustrates the regions of interest selected for analysis. Figure 5.7 illustrates the mean spectra for each region, and Figure 5.8 displays the resultant ratio absorption spectrum for the plume, which has been labeled as stack #1. These results validated the claim that NUVIS had the capability of detecting sulfur dioxide plumes at short range. The image of Figure 5.7 is produced through the Regions of Interest algorithms of the Environment

for Visualizing Images (ENVI) software. Additional ENVI analysis is further detailed in Appendix C.



Figure 5.6. Regions of Interest (ROI's) used to extract sky and plume spectra.

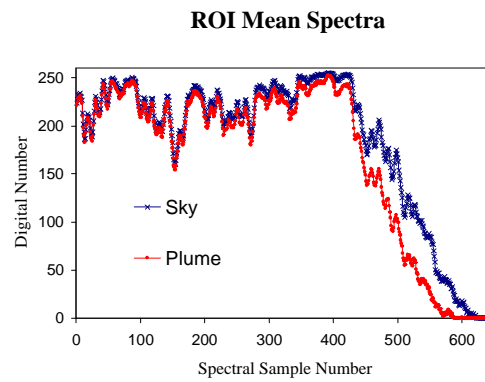


Figure 5.7. ROI mean spectra (see ROI's of Figure 5.6)

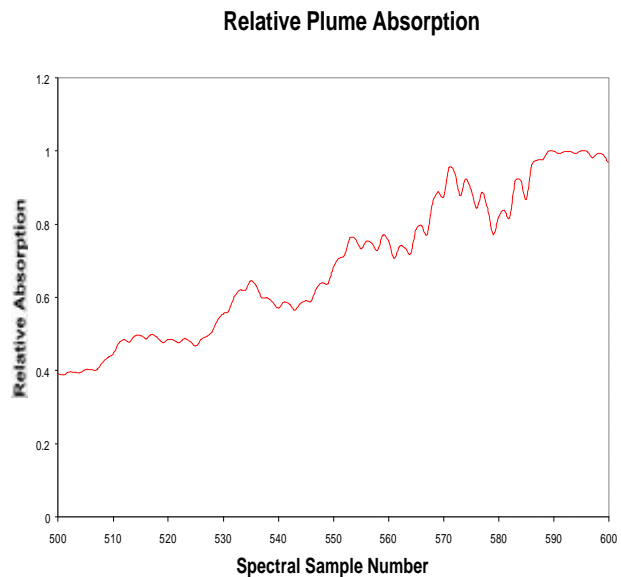


Figure 5.8. Relative plume absorption. (see Figure 5.6)

Applying the same Gaussian curve fitting techniques to this spectrum as were used for the lab data resulted in the curve fit illustrated in Figure 5.9. Equivalent width measurements were made for each of the absorption lines centered at spectral sample numbers 535, 554 and 572, respectively.

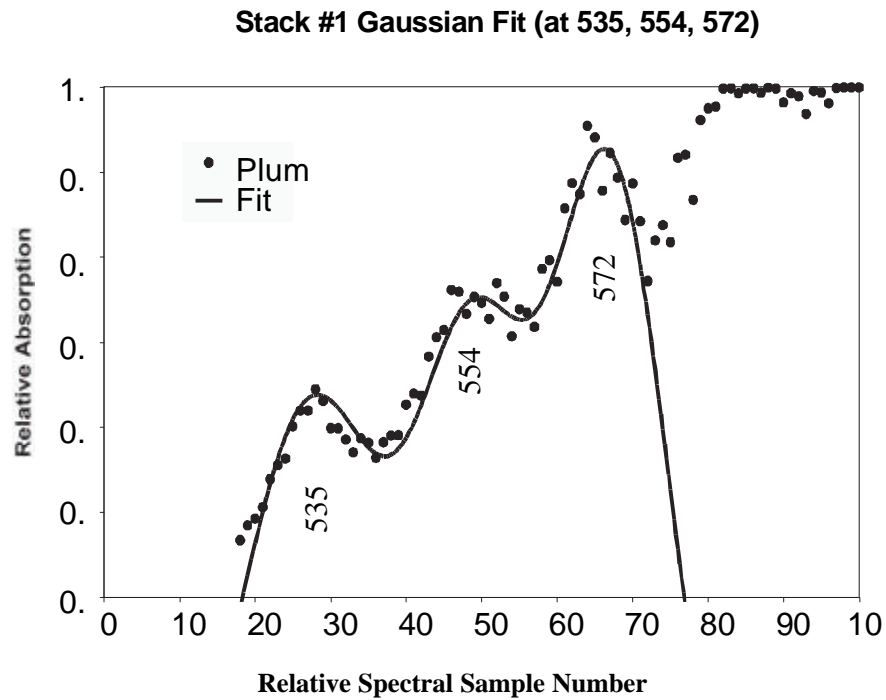


Figure 5.9. Stack #1 Gaussian curve fit.

This resulted in equivalent widths of 1.80, 1.40, and 2.03 nm, respectively. The laboratory curves of growth were then used to deduce the corresponding plume  $\text{SO}_2$  column abundances. Results from this application of the calibration curves to the field data are summarized in Table 5.1.

Spectral Sample Number	Equivalent Width: W (nm)	Column Abundance: $\zeta$ ( $\text{m}^{-2}$ )
535	1.80	$8.88 \times 10^{22}$
554	1.40	$3.42 \times 10^{22}$
572	2.03	$1.60 \times 10^{23}$

Table 5.1. Resultant column abundances of stack #1 from three spectral features.

These are the effective column abundances for the plume, assuming that it is a layer of gas of uniform number density  $n$  and thickness  $L$ , in which case the column abundance would be simply

$$V = n L. \quad (5-1)$$

1)

However, the actual plume geometry is approximately cylindrical, rather than layer-like. So the actual effective absorption path length, assuming a uniform effluent density across the plume of diameter  $D$ , would be the mean thickness of a cylinder of that diameter, as illustrated in Figure 5.10 and in Equation 5-2 where the effective path length is  $L_{eff}$ ,

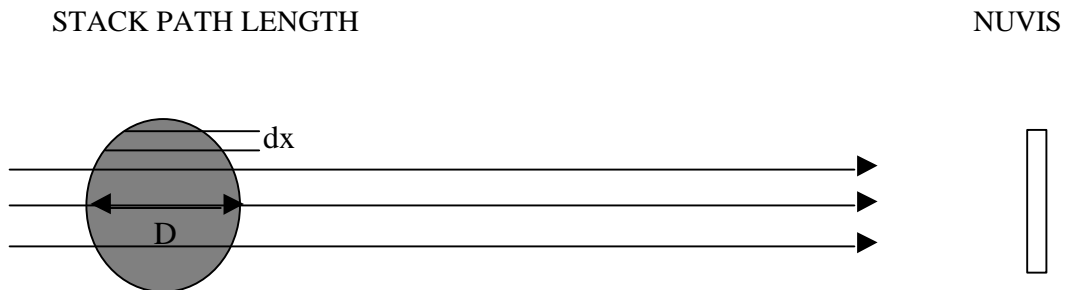


Figure 5.10. Plume geometry.



$$L_{eff} = \frac{\int_{-D/2}^{D/2} 2\sqrt{\frac{D^2}{4} - x^2} dx}{\int_{-D/2}^{D/2} dx} = \frac{pD}{4}. \quad (5-2)$$

Therefore, for a measured column abundance  $V$  across a plume of diameter  $D$ , the number density of  $\text{SO}_2$  in the plume will be

$$n = \frac{V}{L_{eff}} = \frac{4V}{pD}. \quad (5-3)$$

Of course, this assumes that the spectrum was measured along a direction perpendicular to the cylinder axis of the vertical plume (in other words, in a horizontal direction). If the measurement is performed at close range, sighting at an elevation angle  $q$  with respect to the horizontal, then  $L_{eff}$  must be projected along a slant path, giving

$$L_{eff} = \frac{pD}{4 \cos q}, \quad (5-4)$$

from which it follows that the measured  $\text{SO}_2$  number density will be

$$n = \frac{4V \cos q}{pD}. \quad (5-5)$$

When this analysis is applied to the data from Table 5.1, with  $D = 7.6\text{m}$  and  $q = 63$  degrees, it results in the  $\text{SO}_2$  number densities listed in Table 5.2.

Spectral Sample Number	SO <sub>2</sub> Number Density (m <sup>-3</sup> )
535	6.75 x 10 <sup>21</sup>
554	2.60 x 10 <sup>21</sup>
572	1.22 x 10 <sup>22</sup>

Table 5.2. SO<sub>2</sub> number densities with geometric scaling.

The spectrochemical analysis just discussed yielded the plume SO<sub>2</sub> abundance in the form of a number density (i.e. number of molecules per cubic meter of plume gas). However, *in situ* pollution monitoring devices in the stacks express SO<sub>2</sub> concentrations in parts per million (ppm) of stack effluent, a standard unit of measure in the fields of chemical and environmental engineering, called the gas mixing ratio. So, we must convert our spectrochemical measurements to those units if a meaningful comparison is to be made.

Images indicate that cylindrical plumes rise a considerable distance above the tops of the stacks without changing their overall shapes or diameters. This implies that the gas pressure in the flow must be approximately isobaric with the surrounding cool air. This means that, for the comparatively short section of plume observed immediately above the flues, Bernoulli's equation (Halliday and Resnick, 1997) demands that

$$P_{air} = P_{plume} + 0.5 \, r_{plume} \, v_{plume}^2 , \quad (5-$$

6)

where  $P_{air}$  is the hydrostatic pressure of the surrounding cool air,  $P_{plume}$  is the corresponding hydrostatic pressure within the warm plume,  $r_{plume}$  is the mass density of

the plume gas, and  $v_{plume}$  is the plume gas flow velocity with respect to the surrounding air.

The actual situation is, to a good approximation, somewhat simpler than Bernoulli's equation would imply. Since

$$P_{air} \cong 1.0 \times 10^5 \text{ Pa}, r_{plume} \cong r_{air} \cong 1.3 \text{ kg m}^{-3} \text{ and } v_{plume} \cong 10 \text{ ms}^{-1}, \quad (5-7)$$

the magnitude of the hydrodynamic term in Bernoulli's equation is roughly

$$0.5 r_{plume} v_{plume}^2 \cong 65 \text{ Pa}. \quad (5-8)$$

This is much smaller than  $P_{air}$  and so may be neglected in the analysis. So, we have a quasi-hydrostatic system in which  $P_{plume}$  equals  $P_{air}$  to a good approximation.  $P_{plume}$  must be the sum of the partial pressures  $P_{SO_2}$  and  $P_{other}$  of the  $SO_2$  and other effluent constituents, respectively. Assuming that the plume is well mixed and is in thermodynamic equilibrium at absolute temperature  $T_{plume}$ , the ideal gas law (Halliday and Resnick, 1997), when combined with the above results, requires that

$$n_{SO_2} k T_{plume} + n_{other} k T_{plume} = n_{air} k T_{air}, \quad (5-9)$$

where  $n_{SO_2}$ ,  $n_{other}$ ,  $n_{air}$  are the number densities of  $SO_2$ , other plume constituents, and the surrounding air, respectively,  $k$  is Boltzman's constant ( $1.38 \times 10^{-23}$  J/K), and  $T_{air}$  is the absolute temperature of the surrounding air. Therefore, it follows that

$$n_{other} = (n_{air} T_{air} / T_{plume}) - n_{SO_2}, \quad (5-10)$$

and for each spectrochemical measurement of  $n_{SO_2}$ , this formula may be used to calculate  $n_{other}$ . With that number in hand, the measured plume gas mixing ratio

$$n_{SO_2} / n_{other} \quad (5-11)$$

may be estimated and compared with the *in situ* SO<sub>2</sub> measurements. Here are the results:

Spectral Sample Number	$n_{other}$ (m <sup>-3</sup> )	$n_{SO_2} / n_{other}$		Mixing Ratio (ppm)
535	1.967 x10 <sup>25</sup>	3.43 x10 <sup>-4</sup>		343
554	1.968 x10 <sup>25</sup>	1.32 x10 <sup>-4</sup>		132
572	1.967 x 10 <sup>25</sup>	6.20 x10 <sup>-4</sup>		620
Assumed Values:	$n_{air}$ 2.69 x10 <sup>25</sup> m <sup>-3</sup>	$T_{air}$ 300K	$T_{plume}$ 410K	$n_{air}T_{air}/T_{plume}$ 1.968 x10 <sup>25</sup> m <sup>-3</sup>

Table 5.3. Mixing ratio results from observations of stack#1 at 0.2 km.

So the average SO<sub>2</sub> mixing ratio is 365± 200ppm, where the uncertainty is simply the standard deviation about the average. This agrees very well with the *in situ* direct measurements which are near 400 ppm. Because we have only three measurements to work with, the statistics are not overwhelmingly compelling, but the consistency between the two independent measurements is still quite promising.

## VI. CONCLUSIONS AND RECOMMENDATIONS

This thesis research demonstrated conclusively that NUVIS is capable of detecting and quantifying SO<sub>2</sub> emissions in the form of effluent smokestack plumes. This effort entailed two separate phases of research. First, laboratory comparison UV spectra of SO<sub>2</sub> were recorded at different concentrations. These spectra were used to calculate least-squares fitted curves of growth for four different SO<sub>2</sub> spectral features. The curves of growth can now be used for any subsequent spectrochemical measurements of SO<sub>2</sub> column abundances by NUVIS. Second, the results of the laboratory studies were employed to analyze real field data from a coal-burning power plant. Direct *in situ* chemical measurements of the SO<sub>2</sub> in one of the plant's effluent plumes was known to be 400 ppm. Detailed analysis of NUVIS data from the plume yielded a mean plume SO<sub>2</sub> mixing ratio of  $365 \pm 200$  ppm, in excellent agreement with the *in situ* value.

Based upon an assessment of the signal-to-noise ratios in representative field data, and the laboratory observation that SO<sub>2</sub> column abundances must be  $\geq 10^{20} \text{ m}^{-2}$  for NUVIS to detect the SO<sub>2</sub> signatures that we have analyzed, we can estimate the practical lower mixing ratio limit for SO<sub>2</sub> detection in the field. We estimate that it is approximately 70 ppm. This indicates that NUVIS should not have detected quantifiable SO<sub>2</sub> emissions during the 1999 observations of the power plant, when all of the plant's plumes were chemically scrubbed down to SO<sub>2</sub> mixing ratios on the order of 40 ppm. That is indeed the case, further demonstrating the consistency of the experimental and analytical procedures developed during this thesis research project.

A number of steps could be taken to enhance the calibration and analysis techniques outlined in this thesis and to improve the overall sensitivity of the UV hyperspectral remote sensing instrumentation. 1) A new wavelength calibration should be performed. 2) A new set of calibration curves should be developed, involving a wider range of SO<sub>2</sub> concentrations. 3) Repetitive measurements should be made at each location for each scene when in the field in order to check for consistency and to improve upon the signal-to-noise in the data. 4) Further develop and extend the analysis processes presented in Chapters IV and V to include additional spectral features, thereby providing a larger statistical set of measurements. 5) NUVIS should be augmented with peripheral devices to measure all applicable environmental factors (i.e. barometric pressure, temperature, GPS generated position) in conjunction with each field measurement.

As a follow-on to this thesis work, more rigorous analysis should be conducted on the existing field data utilizing the algorithms provided by the ENVI software to more reliably quantify the column densities through a more refined application of this calibration. This process should be further developed through continued field and laboratory experimentation and should also involve corrections for UV foreground scattering and the contributions due to other chemical effluents.

This study has provided an account of NUVIS progression to date. It also demonstrated that sulfur dioxide does exhibit a characteristic ultraviolet absorption signature. It also indicated that the existing instrument was unable to detect SO<sub>2</sub> signatures at concentrations of tens of ppm at long ranges (see Appendix C).

The sensor's resolving power is limited by the eight bit processing capability of the detector, a Pulnix CCD camera. Instrument anomalies (also briefly detailed in Appendix C) can most likely be attributed to optical components such as the scanning mirror and diffraction grating. The anomalies experienced with the processing PC can most likely be attributed to the instrument's software. In either case, further testing is required to fully determine the extent of such anomalies.

Further improvements to the existing instrument could be made to correct many of these problems but a more beneficial approach involves construction of a new instrument, incorporating the lessons learned from NUVIS. It should have higher resolving power and greater sensitivity utilizing a digital twelve/sixteen bit CCD camera, more robust processing power and an improved electronic design that minimizes spurious operational anomalies and glitches. We recommend that further improvements to NUVIS be made, and that a new, more capable instrument be developed and tested with the ultimate goal of someday fielding a similar airborne UV spectral imager.

THIS PAGE INTENTIONALLY LEFT BLANK



## **APPENDIX A. NUVIS FIELD CHECKLIST**

Field experiments involve a great deal of logistics to accomplish a successful mission. Ensuring that NUVIS and all its support components arrive at the site is only one of many concerns during such operations. The following checklist is provided as a material guide for NUVIS field operation. The list is by no means all-inclusive and, depending on the mission at hand may require modifications. Five shipping crates (including pre-designated packing/shipping material: i.e. foam, bubble wrap etc...) are dedicated to the field deployment of NUVIS. Each shipping case will first be listed followed by the recommended contents of each crate:

- CASE #1:

- 1) CPU (IDL HASP may remain in place).
- 2) Monitor (monitor sits firmly against right wall of the shipping crate with foam installed).
- 3) Max-410& JS auxiliary connector terminator.

[Notes: Foam has been specifically cut to specification for packing purposes. Foam pieces are labeled and fit nicely into place to allow shipping of the CPU, monitor and Max-410 remain in one crate. It is recommended that only the foam be removed and that these components remain in the crate during field operation.]

- CASE #2

- 1) NUVIS tripod (with wrench).

- CASE #3

- 1) Spare PC.

- CASE #4

- 1) 25 foot NUVIS umbilical cable.
- 2) 8 foot NUVIS umbilical cable.
- 3) Extension cords (quantity is mission dependent).
- 4) Category 5 cables, blue in color (2 jumpers, 2 network).
- 5) Monitor cable.
- 6) COM1 to Max-410 interface cable.
- 7) UPS.
- 8) Power strip.
- 9) Surge suppressor.
- 10) Mouse.
- 11) Tool kit (screwdrivers, utility knife, wire cutters, pliers, Allen wrenches, etc...).
- 12) Miscellaneous items (paper towels, rope, lens paper, gloves, plastic, etc...).

- CASE #5

- 1) Spare stepper motor.
- 2) Spare Pulnix camera & Lens.
- 3) Spare AZ encoder.
- 4) Spare computer keyboard.
- 5) Spare mouse.
- 6) Spare JAZ drive.
- 7) Spare IDL HASP.
- 8) JAZ Cartridges.
- 9) Diagnostic tools, Fluke, meter and oscilloscope.
- 10) Repair items (tape, cable ties, soldering iron, solder, sponge, spare wire, etc...).
- 11) Documentation (software documentation, Keithly, US Digital and Max-410 docs.).
- 12) Backup discs (operating system, software, hard drive, etc...).
- 13) Gas test cells.
- 14) Spare camera.

## APPENDIX B. NUVIS OPERATIONAL CHECKLIST

### SETTING UP THE SYSTEM

- #1 Remove tripod from case and set in place. Use key (stored at the base of the tripod) to move instrument locking mechanism from its slot by unlocking the setscrew.
- #2 Remove instrument from case and slide instrument into place on the tripod mounting plate. Once instrument is in place, reset locking mechanism and retighten set-screw. (Key may be restowed.)
- #3 Remove protective cover from optical sight. It is recommended that the window cover not be removed until system is fully operational. This will provide maximum protection to the filter window.
- #4 Ensure computer system components are accessible. Currently it is recommended that the computer components and stepper motor remain in the carry case with only the two access covers removed. This provides maximum protection and ease of mobility while all components remain readily accessible.
- #5 Connect the UPS to the appropriate source of power (115 VAC outlet or field generator). Connect the computer, monitor, Ethernet hub and stepper motor controller power cables to each component and to the UPS. Ensure that the voltage switch on the computer is set to 115 volts.
- #6 Connect monitor cable, mouse and keyboard to the PC.
- #7 Now connect the remaining cables including NUVIS umbilical cables and blue category five cables. Connections are to be made to the various cable connectors on the NUVIS instrument as well as to the AMS 410 and rear panel of the PC. Figure B.1 illustrates these connections.

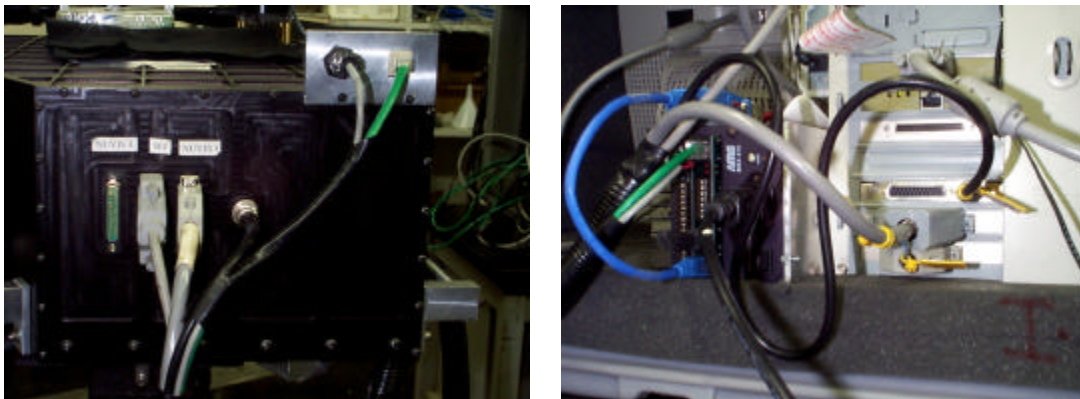


Figure B.1. NUVIS umbilical, instrument, PC and AMS-410 cable connections.

## GETTING UP AND RUNNING

(You should now be ready to power up the system.)

#1 Turn on the monitor and PC. (To turn on PC ensure switch on back panel is set to the on position and then push, turn and release blue switch on the front panel of the PC.)

#2 Wait for the BIOS display and initial indication that the operating system (Windows 95) is functioning. This will take some time.

#3 Once this is complete, the standard 'Enter Network Password' screen will appear. If networking is desired, enter appropriate password, otherwise press 'escape.' In either case, the standard Windows screen with short-cut icons will next appear.

DO NOT LAUNCH THE *NUVIS.EXE* PROGRAM  
UNTIL COMPLETING STEPS SIX THROUGH EIGHT:

#6 Turn on the stepper motor controller.

#7 Once this is accomplished and you are ready to take data, remove the protective cover from the NUVIS window. (If the 4inch test cell is required, install the mounting studs, install the cell, and secure the cell in place with the stud nuts.) Align the instrument as required.

#8 The *NUVIS.EXE* program is memory intensive. Close all other applications before launching this program. It is actually recommended that NO OTHER APPLICATIONS BE OPENED PRIOR TO LAUNCHING *NUVIS.EXE*. If a number of applications had been previously opened, it might be wise to shut down the PC and restart. This will dedicate the PC to NUVIS operation only. Once this is complete, you are now ready for NUVIS operation.

## INSTRUMENT OPERATION WITH *NUVIS.EXE*

#1 Launch the *NUVIS.EXE* program.

#2 Upon execution of the program, four windows will appear on the monitor prior to the presentation of the actual operational window. These windows are detailed in Table B.1.

SEQUENCE	WINDOW STATEMENT	DESCRIPTION/ REQUIRED ACTION
1)	Is Max-410 Ready?	This is a reminder. As long as Max-410 is on, enter OK.
2)	Mirror is aligned.	Once previous step was completed, the Max-410 ensured communications with the instrument and centered the mirror to position zero. This statement confirms that action. Enter OK.
3)	Blank	Blank Window. Enter OK
4)	Based on memory, # frames is XXX. (i.e. 613)	This indicates the number of images that may be stored in RAM. If this number is below 400, another application was most likely previously opened. Before proceeding, it is best to restart the sequence to ensure enough memory is available. Otherwise, Enter OK.

Table B.1. Window sequence upon execution of the *NUVIS.EXE* program.

#3 Once the above sequence is completed, the operational window of Figure B.2 is obtained and preparation for an actual data collection is nearly complete.

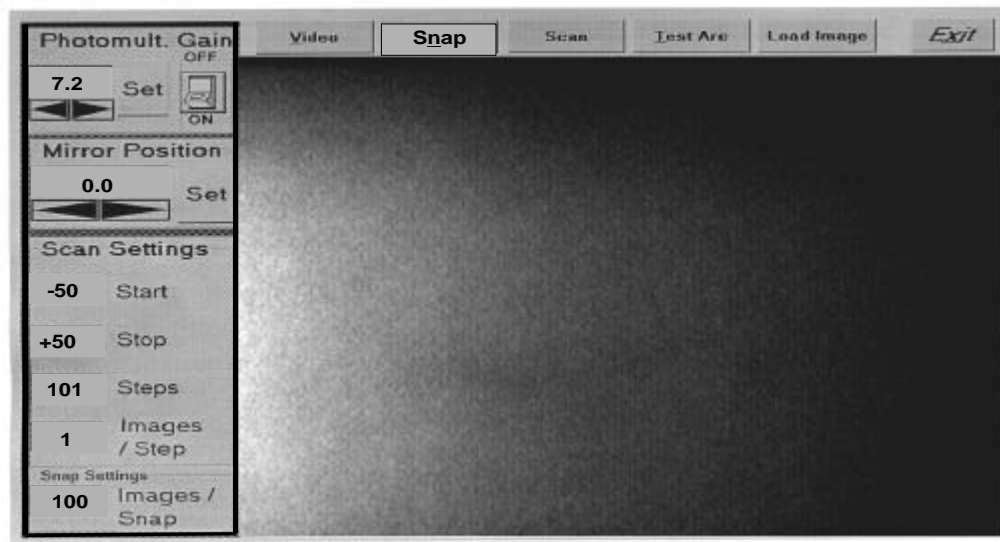


Figure B.2. NUVIS operational Window.

(If any problems are encountered prior to this point, it is best to exit the program and restart the process. If memory was initially low, this may require a complete system shutdown and restart. If the program screen locks up during portion of the startup sequence, the 'ctrl-alt-del' command to end the task may not be available. If this occurs, do not attempt to use this command a second time to restart your computer. This method of rebooting (once the NUVIS.EXE program is executed) may cause damage to certain Windows operating files. As a last resort, if the program locks up, try to turn the system power off manually and restart the system. Normal system shutdown is detailed in the final steps of this procedure. Likewise, when exiting the NUVIS.EXE program, it is best to perform a proper system shutdown every time. This requires using the EXIT button appearing in the operational control window.

#4 Set the *Photomultiplier Gain*. It is best to start at a lower value (5.0 or below) to begin. Gains may be set from 0 to 10 by keyboard entry or by using the arrows and mouse.

#5 Assuming that the instrument is pointed at the appropriate target, a quick-look at the sensor's active digital signal may be obtained by activating the VIDEO button. The brighter pixels correspond to higher digital signals. Keeping in mind that the detector should not be saturated, the image intensifier should be adjusted until an appropriate signal is displayed. The image intensifier must also first be turned ON prior to selecting the VIDEO button or either of the two modes described in the steps that follow. Also, keep in mind that the screen display does not represent the image scene directly as viewed from behind the instrument. The screen display is actually inverted from the scene itself.

#6 Prior to collecting data, ensure that there is enough memory available on the harddrive and/or ensure that a JAZ cartridge is installed for data collection.

#7 *Mirror Position* (center position) may be set through the active window. This number should initially be zero since the mirror was centered during the startup sequence.

#8 Two operational modes exist with NUVIS: (1) SNAP and (2) SCAN. The following information should be reviewed before selecting either one of these modes:

(1) SNAP:

*Images/Snap*. This setting determines the successive number of SNAPS to be performed. During a NUVIS SNAP, the mirror remains centered on the position of step #7.

(2) SCAN:

The *Start* and *Stop* settings only apply to the SCAN function. Setting mirror *Start* and *Stop* positions automatically resets the number of steps through which the mirror will scan. The number of steps can only be controlled by the start and stop settings. A maximum of 351 steps may be utilized but steps in excess of 200 may cause system failures due to memory allocation faults.

The number of *Images/Step* may also be selected. This defines the number of SNAPS to be performed at each repositioning of the mirror

A NUVIS "SNAP" is simply a 640 x 480 byte array of data achieved through the instrument control program. Each individual SNAP may be written to either the PC's hard drive or internal JAZ drive and will register as a 300KB file if only one frame is obtained. One frame is simply a two-dimensional set of data representing the spectral (wavelength) and spatial (vertical) components of the representative scene. Although this frame of data is not really an image, the operational NUVIS window refers to it as such.

Selecting multiple images per SNAP (i.e. 100), will increase the size of the data file as 100 different 640x480 byte arrays are written, one by one, to the either of the available drives as a complete data file. This is the preferred mode of operation during an instrument calibration when the entire field of view of the instrument is uniformly focused on a standard gas test cell and not a true image scene. These multiple SNAPS may be averaged during the analysis process to improve signal to noise. A file containing 100 "images per SNAP" is normally 30MB in size. With these settings, a data file smaller than 30MB indicates a problem with that particular collection.

A NUVIS "SCAN" is a bit different. It is the preferred method when an image scene is being targeted. By selecting the mirror stop and start positions in the instrument control window (see Appendix B) the operator sets the number of steps (i.e. scan line numbers) through which the mirror will scan. The mirror, which is first centered at position zero during startup, is moved to the initial offset position (i.e. start position) and begins to scan. It rotates through the specified number of steps until reaching the magnitude of the same offset position (i.e. stop position) at the end of the scan. The number of images per step may also be set by the operator. Typical settings for a routine SCAN include start/stop values of -50 to +50, which corresponds to 101 different steps or mirror positions. Approximately 300KB of data storage is required for each step. As demonstrated by each of these operational modes, NUVIS data files are quite large requiring that the CPU be fully dedicated to the reading/writing of this data once a data collection has been initiated. This is a major restriction imposed by the current *NUVIS.EXE* program that is written in Visual Basic.

#9      Select the appropriate mode: SNAP or SCAN.

#10     Once the mode is selected and executed, the reading and writing of sensor data will take a considerable amount of time (30 to 120 seconds in most cases). The program will ask for a file name in which to store the data. The customary file extension used in all NUVIS files is a '.nuv' extension. The file will be saved in JPEG format.

#11     It is highly recommended that one operation be fully completed before the next command is issued. It is best to be patient, as the program has its own inherent limitations and is not as streamlined as many of the commercial software applications on the market. System operators should ensure that only one function at a time is requested to reduce the possibility of program failures.

#12     As previously mentioned, to exit the system use the *EXIT* button.

The *TEST ARC* and *LOAD IMAGE* buttons are not functional.



## **APPENDIX C: RANGE EFFECTS AND NUVIS ANOMALIES**

Data presented in this section were taken from the 1998 field trip to the coal burning power plant. Figure C.1 illustrates the scene in a principle components format. A principle components transform on bands 500 to 640 reduces the data to this image, which highlights the differences between the clean and dirty plumes. A brief analysis of the plumes is done with eight regions of interest at a range of 1.5 km. These regions are illustrated in Figure C.2. The ratioed relative absorption spectra are displayed in Figure C.3, demonstrating not only the effects of range on the detected spectra but also providing a comparison of the signatures of the scrubbed and unscrubbed stacks at this range.

A very preliminary analysis of these data was conducted using a matched filter technique. Because the absorption lines for the clean stacks were not being unambiguously detected by the instrument at range, this approach was tried in order to improve the detection of SO<sub>2</sub> signatures. The matched filter technique utilized in scene spectra for both the sulfur dioxide and the sky background. The results of this technique are displayed in Figures C.4 and C.5. In Figure C.4, apparent regions of SO<sub>2</sub> are indicated by the dark regions in the display. This particular scene includes the unscrubbed stack at a range of 1.5km. A similar matching technique resulted in pixel matching in the modeled sky spectrum as illustrated by the lighter regions of Figure C.5.

**3 Stacks - 1.5 km**  
**Principal Components**  
 Cyan: PC1    Red: PC2

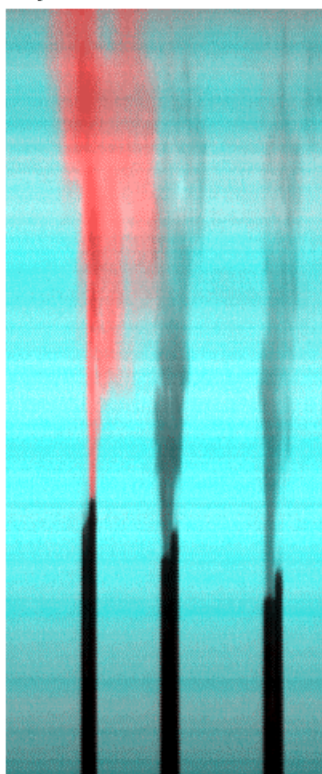


Figure C.1. Principle components image taken from bands 500-640 of the original data set. Principal component 1 is encoded as cyan (green/blue guns), principal compent 2 is encoded as red.

**Regions of Interest**  
**at 1.5 km**

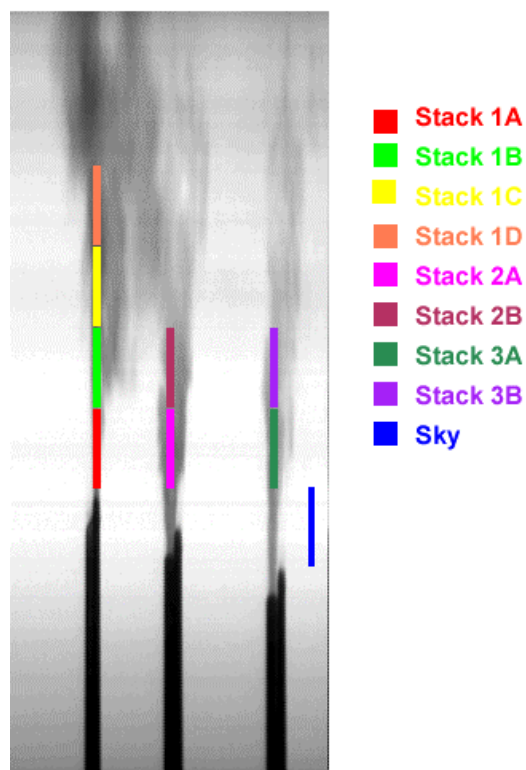


Figure C.2. Principle component 1 image with regions of interest superimposed. Color codes correspond to the mean spectra in Figure C.3.

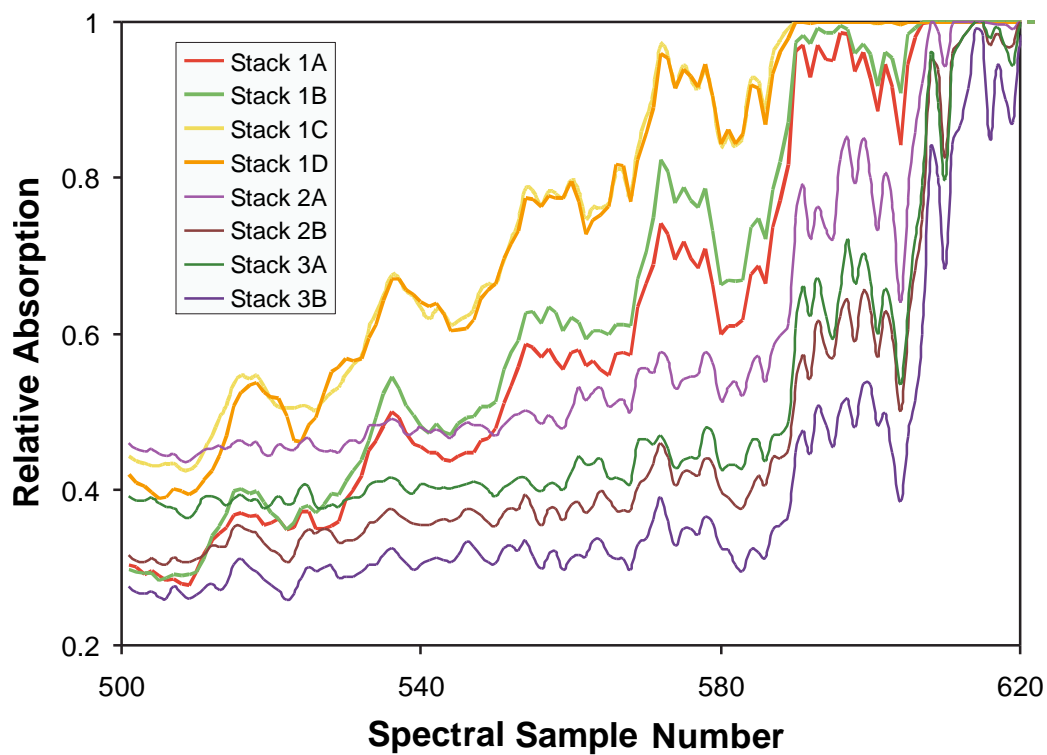


Figure C.3 Relative Absorption Spectra for regions of interest at 1.5 km.

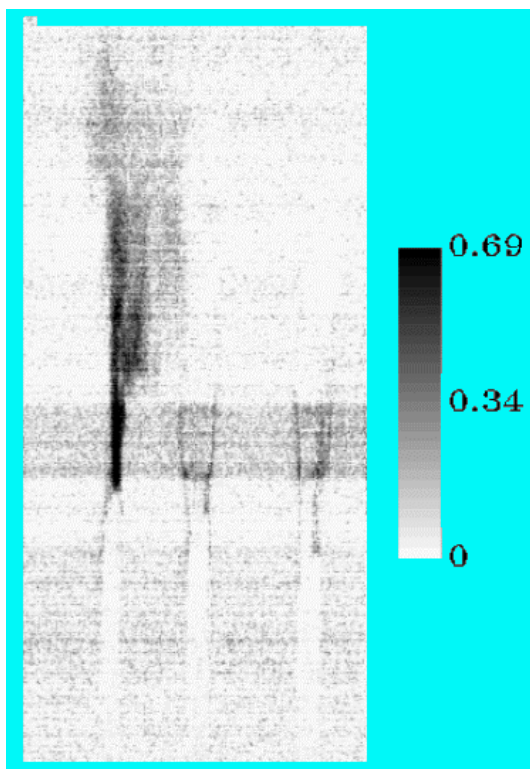


Figure C.4. SO<sub>2</sub> matched filter. Scale indicates relative match.

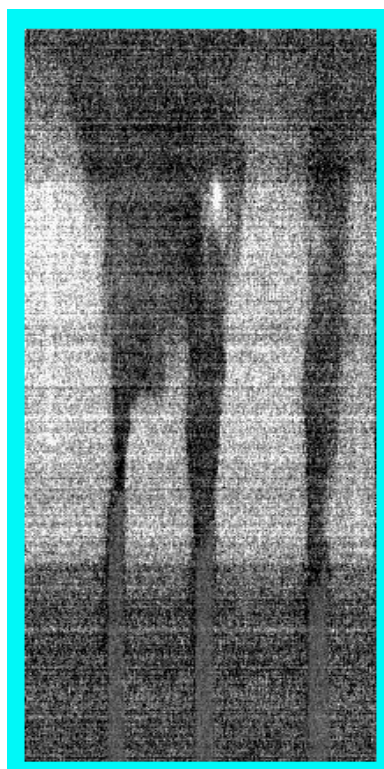


Figure C.5. Sky matched filter.

THIS PAGE INTENTIONALLY LEFT BLANK

## LIST OF REFERENCES

- Aitken, P., *Visual Basic 5 Programming Explorer*, The Coriolis Group, Inc., 1997.
- Atkins, P.W., *Physical Chemistry*, Fourth Edition, W.H. Freeman and Company, New York, New York, 1990.
- Cleary, D.D., Private Conversation, (1998).
- Durkee, P.A., “MR 3480 – Thermodynamic and Radiative Processes in the Atmosphere”, <http://www.met.nps.navy.mil/~durkee/MR3480/MR3480.htm>, 1999.
- Eisberg, R., and Resnick, R., *Quantum Physics of Atoms, Molecules, Solids, Nuclei, and Particles*, Second Edition, John Wiley and Sons, New York, New York, 1985.
- Finlayson-Pitts, B.J., Pitts, J.N. Jr., *Atmospheric Chemistry: Fundamentals and Experimental Techniques*, John Wiley and Sons, New York, New York, 1986.
- Haliday, D., Resnick, R., Walker, J., *Fundamentals of Physics Extended*, Fifth Edition, John Wiley and Sons, New York, New York, 1997.
- Hecht, E., *Optics*, Third Edition, Addison-Wesley Longman Inc., Reading, Massachusetts, 1998.
- Hooks, T.A., “Design Construction and Operation of the Naval Postgraduate School’s Ultraviolet Imaging Spectrometer (NUVIS)”, Master’s Thesis, Naval Postgraduate School, Monterey, California, (1997).
- Johnson, E.O., “Design Development and Testing of an Ultraviolet Hyperspectral Imager”, Master’s Thesis, Naval Postgraduate School, Monterey, California, (1996).
- Kramer, H.J., *Observations of Earth and Its Environment*, Third Enlarged Edition, Springer-Verlag, Berlin, Germany, 1996.
- Lenoble, J., *Atmospherics Radiative Transfer*, A. Deepak Publishing, Hampton, Virginia, 1993.
- MacMannis, A.R., “The Design of the Naval Postgraduate School’s Ultraviolet Imaging Spectrometer (NUVIS)”, Master’s Thesis, Naval Postgraduate School, Monterey, California, (1997).
- Multispectral Users Guide*, Department of Defense, August, 1995.

Skoog, D.A., *Principles of Instrumental Analysis*, Third Edition, Saunders College Publishing, Philadelphia, Pennsylvania, 1985.

Strickland, D.J., and Bishop, J., *Remote Sensing of Tropospheric SO<sub>2</sub> from Space*, Computational Physics Inc., Fairfax, Virginia, 1999.

Thorne, A., Litzen, U., and Johansson, S., *Spectrophysics: Principles and Applications*, Springer-Verlag, Berlin, Germany, 1999.

United States Geological Survey(USGS), "Description: COSPEC Measurements", [http://vulcan.wr.usgs.gov/Monitoring...scriptions/description\\_COSPEC.html](http://vulcan.wr.usgs.gov/Monitoring...scriptions/description_COSPEC.html), 1999.

*Using IDL, IDL Version 5.0*, Research Systems Inc., Boulder, Colorado, 1997.

## INITIAL DISTRIBUTION LIST

1. Defense Technical Information Center ..... 2  
8725 John J. Kingman Road., Ste 0944  
Fort Belvoir, VA 22060-6128
  
2. Dudley Knox Library..... 2  
Naval Postgraduate School  
411 Deyer Rd.  
Monterey, CA 93943-5101
  
3. David S. Davis Code PH/DV..... 2  
Department of Physics  
Naval Postgraduate School  
Monterey, CA 93943-5101
  
4. Richard C. Olsen Code PH/OS ..... 5  
Department of Physics  
Naval Postgraduate School  
Monterey, CA 93943-5101
  
5. Chairman, Code PH ..... 2  
Department of Physics  
Naval Postgraduate School  
Monterey, CA 93943-5101
  
6. Curricular Officer, Code 34 ..... 1  
Engineering and Technology  
Naval Postgraduate School  
Monterey, CA 93943-5107
  
7. Tamir Elias..... 1  
U.S. Geological Survey  
Hawaiian Volcano Observatory  
Hawaii National Park, HI 96718
  
8. Willie Williams ..... 1  
14675 Lee Road  
Chantilly, VA 20151-1715

9. Lieutenant Michael Rigo..... 1  
4675 Lee Road  
Chantilly, VA 20151-1715
10. Greg Pavlin ..... 1  
SITAC  
11781 Lee Jackson Memorial Highway, Suite 500  
Fairfax, VA 22033-3309
11. Mr. Stephen A. Marino..... 2  
3215 Concord Drive  
New Castle, PA 16105
12. Major Stephen Finney..... 2  
346 Summerwood Lane  
Castle Rock, CO 80104
13. Dr. David D. Cleary ..... 2  
2901 W. 96<sup>th</sup> Street  
Bloomington, MN 55431